Precipitation in the mountains of Central Asia: isotopic composition and source regions

Zarina Saidaliyeva[1], Maria Shahgedanova[1], Vadim Yapiyev[1,2], Andrew John Wade[1], Fakhriddin Akbarov[3], Mukhammed Esenaman uulu[4], Olga Kalashnikova[4], Vassiliy Kapitsa[5], Nikolay Kasatkin [5], Ilkhomiddin Rakhimov[6], Rysbek Satylkanov[7], Daniiar Sayakbaev[7], Eleonora Semakova[8], Igor Severskiy[5], Maxim Petrov[3], Gulomjon Umirzakov[9,10], and Ryskul Usubaliev[4]

[1]Department of Geography and Environmental Science, University of Reading, Reading, RG66AB, UK;
[2]School of Mining and Geosciences, Nazarbayev University, Astana, 010000, Kazakhstan
[3]Institute of Geology and Geophysics, Tashkent, 100164, Uzbekistan;
[4]Central-Asian Institute for Applied Geosciences, Bishkek, 720027, Kyrgyzstan;
[5]Central Asian Regional Glaciological Centre Under the Auspices of UNESCO, Almaty, 050010, Kazakhstan;
[6]Institute of Water Problems, Hydropower and Environment, Dushanbe, 734025, Tajikistan;
[7]Tien-Shan High Mountain Scientific Centre, Bishkek, 720033, Kyrgyzstan;
[8]Ulugh Beg Astronomical Institute of the Uzbekistan Academy of Science Tashkent, 100052, Uzbekistan;
[9]National University of Uzbekistan, Tashkent, 100174, Uzbekistan;
[10]Hydrometeorological Research Institute, Tashkent, 100052, Uzbekistan

Correspondence to: Zarina Saidaliyeva (z.saidaliyeva@pgr.reading.ac.uk)

Abstract. Over 900 event-based precipitation samples were collected in 2019–2021 in the Tien Shan and its foothills and analysed using cavity ring-down spectroscopy. δD and $\delta^{18}O$ values were highest in summer and lowest in winter, and annual cycles of d-excess varied between sites reflecting local conditions. The $\delta^{18}O$ and δD values increased from north to south in all seasons except autumn, and latitude was a statistically significant predictor of $\delta^{18}O$ and δD in the overall data set along with elevation in winter, and elevation and longitude in autumn. Elevation was a significant predictor of d-excess in all seasons, and local air temperature was a more important control over $\delta^{18}O$ and δD than precipitation depth. Local Meteoric Water Lines were derived using seven regression methods applied to non-weighted and weighted precipitation. Non-weighted Ordinary Least Squares Regression and Reduced Major Axis Regression methods are recommended overall, except for summer when the-Precipitation-Weighted Least Squares Regression should be used, particularly in the south. Atmospheric back trajectory and mixing model analyses were applied in combination to identify air-mass source-regions, and their relative contribution, to precipitation. Recycled moisture from irrigated land in the Amu Darya and Syr Darya basins and from the study catchments accounted for 29–71% of precipitation, depending on site and season. In the Chon-Kyzyl-Suu catchment, local re-evaporation from Lake Issyk Kul, accounted for up to 85% of precipitation. These findings highlight the importance of moisture from terrestrial sources, especially irrigated land, for the formation of precipitation in the Tien Shan.

1 Introduction

Atmospheric precipitation is the primary water source that contributes to river runoff in the mountains of Central Asia (CA), both directly and by sustaining seasonal snowpack and glaciers, whose meltwater maintains dry-season river flow. In CA, precipitation is characterised by strong spatial variability due to large changes in elevation, from approximately 400 to 7000 m above sea level (a.s.l.) over relatively short distances, and the mountain ridge and valley positions in relation to the moisture-bearing flow (Lydolph, 1977; Aizen et al., 1997). Longer-term changes and interannual precipitation variability affect all components of CA water resources (Shahgedanova, 2002; Jin et al., 2012; Aizen et al., 2017), and there is strong evidence for a decline in glacier area and negative glacier mass balance (Kutuzov and Shahgedanova, 2009; Farinotti et al., 2015; Severskiy et al., 2016; Kapitsa et al., 2020). These changes are attributed to the observed air-temperature increase and to prolonged negative precipitation anomalies observed in the 1970s-1980s (Shahgedanova et al., 2018; Hoelzle et al., 2019). Projections

from the Coupled Model Intercomparison Project Phase 6 (CMIP6) show an increase in annual precipitation in high mountain regions, with variation between regions and seasons - especially over the plains and foothills, and uncertainty remains about

45 how these changes will be offset or enhanced by changes in evaporation and atmospheric circulation (Jiang et al., 2020). These uncertainties are amplified in impact assessments using glacier mass balance, hydrological, water resource, and crop models. To reduce the uncertainties in the precipitation projections, a better understanding of precipitation sources and moisture cycling, the links between changes in atmospheric circulation and precipitation, and of the precipitation response to climatic warming, is needed (Kaser et al., 2010; Immerzeel et al., 2020; Viviroli et al., 2020).

50 Analysis of the isotopic composition of precipitation has been used to investigate precipitation sources and moisture cycling (Yoshimura, 2015; Putman et al., 2019; Jasechko, 2019), as the stable isotopes of hydrogen and oxygen describe water fractionation due to evaporation, transportation and condensation, and precipitation. The ratios of heavy (^{18}O) to light (^{16}O) isotopes of oxygen (δ^{18}O) and deuterium (D) to light hydrogen (^{1}H) and the relationship between δD and δ^{18}O in precipitation at the global scale, known as Global Meteoric Water Line (GMWL) and approximated by Equation (1), have been widely

55 applied in hydrometeorology since the 1960s (Craig, 1961; Craig and Gordon, 1965):

$$\delta D = 8 \times \delta^{18}O + 10 \tag{1}$$

Rozanski et al. (1993) investigated δD and δ^{18}O relationships using the data from the Global Network of Isotopes in Precipitation (GNIP) sites and suggested that Local Meteoric Water Lines (LMWL) provide a better representation of isotopic composition of regional precipitation because they depend on latitude, continentality, altitude, and regional climatic anomalies.

60 Relationships between GMWL and LMWLs help identify regional characteristics and processes affecting precipitation (Wang et al., 2018; Putman et al., 2019). LMWLs are typically used together with the deuterium excess (*d-excess*). Equation (2) was developed by Dansgaard (1964) to define *d-excess* and is used to characterise moisture sources:

$$d\text{-}excess = \delta D - (8 \times \delta^{18}O) \tag{2}$$

The global average *d-excess* of precipitation is 10‰. In general, moisture recycling increases *d-excess* values and higher *d-*

65 *excess* in precipitation signifies the addition of re-evaporated moisture from continental basins, while lower values signify moisture originating from the oceans. This difference makes it possible to distinguish precipitation originating over the distant oceanic sources and more local sources in the continental interiors (Araguás-Araguás et al., 2000; Pang et al., 2011; Aemisegger et al., 2014; Bershaw, 2018) particularly when *d-excess* is used in conjunction with atmospheric back-trajectory analysis (Wang et al., 2017, 2019; Bershaw, 2018). Sub-cloud evaporation in a warm and dry air column reduces *d-excess*

70 (Friedman et al., 1962) and *d-excess* of cloud condensate may be substantially different from the *d-excess* of precipitation samples collected at ground level (Froehlich et al., 2008) especially in arid regions (Juhlke et al., 2019). Isotopic composition and *d-excess* can also change with altitude (Bershaw, 2018; Natali et al., 2022; Yang et al., 2023) in response to sub-cloud evaporation, variations in distances travelled by a raindrop, and the transition from upwind slope, where lower temperature and higher humidity supress evaporation as orographic precipitation forms, to downwind rain shadow. While the sub-cloud

75 evaporation and a shorter distance travelled by a raindrop are known to decrease *d-excess* values, the rain shadow effect results in higher *d-excess*. Consequently, *d-excess* serves as a valuable proxy for not only identifying precipitation sources but also for tracking changes in air mass moisture along its pathway.

While the use of stable isotopes in hydrometeorology increases globally (Yoshimura, 2015; Aggarwal et al., 2016; Jasechko, 2019), knowledge about the isotopic composition of precipitation in CA (defined here as Kazakhstan (KZ), Kyrgyzstan (KG),

80 Tajikistan (TJ), Turkmenistan, and Uzbekistan (UZ)) is limited. Currently, the GNIP database contains only seven measurements of δD and δ^{18}O from the precipitation samples collected in Tashkent, Uzbekistan (IAEA/WMO, 2015). This contrasts to extensive measurements in the Chinese Tien Shan (Pang et al., 2011; Wang et al., 2016b, 2018; Chen et al., 2021)

where the Chinese Network of Isotopes in Precipitation (CHNIP) became operational in 2004 (Liu et al., 2014; Zhang and Wang, 2018).

85 The lack of CA precipitation isotope data prevents LMWL development and limits the understanding and quantification of the regional contributions to precipitation. In contrast to the Chinese Tien Shan where events-based precipitation samples were analysed (Pang et al., 2011; Wang et al., 2016b, 2018; Chen et al., 2021), in CA, isotopic compositions from ice-cores taken from the Inylchek (Tien Shan) and Fedchenko (Pamir) glaciers only have been used to characterise moisture sources and regional atmospheric circulation patterns (Aizen et al., 1996, 2004, 2009; Kreutz et al., 2003). Moisture sources for the Inylchek

90 glacier were established broadly as the Atlantic Ocean, Mediterranean and Black Seas on the basis of $\delta^{18}O$ analysis combined with the catalogue of weather types (Aizen et al., 2004), whilst most precipitation over the Pamir originated in the Atlantic (Aizen et al., 2009). The dominant moisture sources for the western Pamir were identified as the Mediterranean and Caspian Seas, which was further evidenced by high *d-excess* values of 20‰ measured in snow and ice cores (Bershaw, 2018). However, according to the event-based precipitation and trajectory analyses, *d-excess* in the western Pamir was lower at 13‰

95 leading to the conclusion that the Mediterranean contributed approximately 20% of the total moisture (Juhlke et al., 2019). This discrepancy may be due to the uncertainty in linking ice core samples to moisture trajectories, or because regional source signals are altered in CA along the long moisture transportation routes (Bershaw, 2018).

The overall aim of the work is to determine the air-mass source-regions and trajectories of the precipitation falling over the northern Tien Shan with the purpose to improve knowledge of this aspect of the regional link between precipitation and water

100 resources. To achieve the overall aim there are four objectives to: (i) evaluate the spatial and temporal variations in the isotopic composition of precipitation; (ii) quantify the relationship between $\delta^{18}O$ and δD and location, air temperature, and precipitation depth; (iii) derive LMWLs, and (iv) establish a relationship between variations in isotopic composition of precipitation and air mass origin. Objectives one, two and three are set to help better understand the atmospheric and geographical controls on precipitation isotope ratio variability in space and over time. The derivation of LMWLs (objective three) has the benefit of

105 aiding the future assessment of the relative contributions of different water sources to streamflow, groundwater recharge, and isotope mass-balance studies. We combined a backward trajectory analysis with isotopologue data to explore the utility of the latter for determining the relative contribution of different air-mass source-regions to the regional mountain precipitation. To achieve the objectives and hence the overall aim, water stable isotopes were measured in precipitation samples between 2019 and 2021 by the Central Asia Research and Adaptation Water Network (CARAWAN) in five catchments located

110 predominantly in the mountains (Fig. 1).

2 Data and methods

2.1 Study area and sampling programme

Precipitation samples were collected in five river catchments: Ulken Almaty (UA), Ala-Archa (AA), Chon Kyzyl-Suu (CKS), and Chirchik (CHK) in the Tien Shan, and the Kofarnihon (KF) in the Pamir-Alai (Fig. 1a). CKS is located on the shores of

115 Lake Issyk Kul, the largest fresh-water mountain lake in CA which does not freeze in winter. There is a smaller lake, which freezes in winter, in proximity to UA1 site. There were eight sampling sites six of which were in the mountains between 1255 and 3277 m a.s.l. and two in the foothills at lower elevations (Table 1).

In the UA, AA and CKS catchments in the north of the region, the Köppen climate classification is subarctic and tundra in the high mountains changing to humid-continental climate in the middle mountains and to the semi-arid grassland steppe as

120 elevation decreases. In the CHK and KF catchments in the south, the Köppen climate classification changes with elevation from subarctic in the high mountains to humid-continental, then to a Mediterranean climate and to semi-arid grasslands and desert on the plains. The region is characterised by the strong seasonal and altitudinal changes in temperature and precipitation

(Fig 1b, c). In the foothills, mean July temperatures reach 24-26°C and mean January temperatures vary between approximately –10°C in the north and 5°C in the south of the region. Annual precipitation ranges between 100 mm a^{-1} in the deserts of

125   Uzbekistan and southern-western Kazakhstan to 1200 a^{-1} mm in the mountains. The location of the major mountain ranges is an important control over precipitation and, while the outer ranges receive high precipitation during the wet season, intermontane basins are arid (Lydolph, 1977; Aizen et al., 1997). Precipitation increases in October when regional atmospheric circulation is dominated by the westerly flow. Across most of the region, precipitation maxima occur in spring, in March – April in the south and April – May in the north. At higher elevations in the northern Tien Shan, precipitation peaks between

130   May and July (Fig. 1c). In winter, the northern part of the region is dominated by the Siberian anticyclone and precipitation is low.
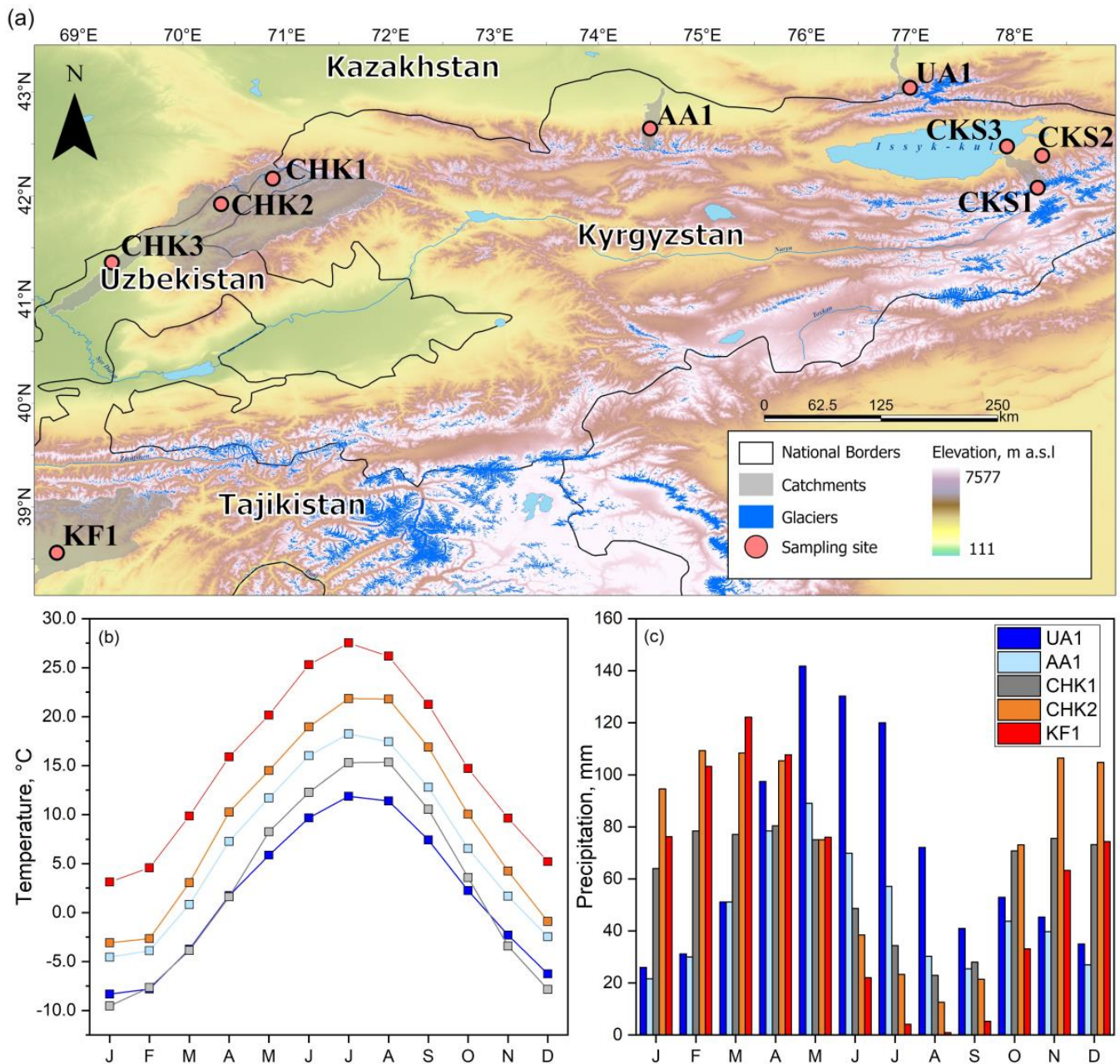
Figure 1: (a) Study area and locations of the sampling sites. Site numbering and details are given in Table 1. A Digital Elevation

135   Model (DEM) derived from the Shuttle Radar Topography Mission (SRTM) is used as background (available from https://lpdaac.usgs.gov/about/citing_lp_daac_and_data). Glacier outlines are from the Global Land Ice Measurements from

Space (GLIMS) database (Consortium, 2017). National borders and water bodies are from ESRI ArcGIS Hub. (b) Mean monthly temperature and (c) mean monthly precipitation in the 1980-2015 period.

140   The event-based precipitation samples (n = 908) and meteorological data (daily air temperature; depth, type and duration of event-based precipitation) were collected between 2019 and 2021 (Table 1). Seven samples of cumulative monthly precipitation were collected in Dushanbe using a PALMEX rain sampler (http://www.rainsampler.com/portfolio-page/rain-sampler-rs1/).

145   Table 1: Characteristics of sampling sites (Fig. 1a) and details of the sampling programme. N is number of samples.

Site code	Sampling sites	Catchment	Country	Lat (N)	Lon (E)	Elevation (m a.s.l)	Period	N	N with precipitation depth data
UA1	Bolshoe Almatinskoe Lake (BAL)	Ulken Almaty (UA)	KZ	43.04	76.99	2563	May 2019 - October 2021	338	332
AA1	Baityk	Ala-Archa (AA)	KG	42.65	74.50	1588	July 2019 - May 2021	115	115
CKS1	Karabatkak Glacier		KG	42.16	78.27	3277	August 2019 - August 2021	37	35
CKS2	Lesnoy Cordon	Chon Kyzyl-Suu (CKS)	KG	42.19	78.20	2571	May 2019 - August 2021	117	114
CKS3	Tien-Shan High Mountain Scientific Centre (TSC)		KG	42.35	78.02	1775	February 2020 - July 2021	29	-
CHK1	Oygaing		UZ	42.00	70.64	1490	Junuary 2020 - October 2021	196	196
CHK2	Pskem	Chirchik (CHK)	UZ	41.92	70.37	1255	November 2020 - July 2021	30	30
CHK3	Tashkent		UZ	41.36	69.32	486	November 2020 - October 2021	46	46
KF1	Dushanbe*	Kofarnihon (KF)	TJ	38.56	68.79	816	October 2018 - October 2019	7	6
			Total					915	874

*Cumulative monthly precipitation

The event-based precipitation samples were collected using the standard Tretyakov rain gauges immediately after the precipitation events by the trained meteorological observers who were ever present at the sites for the duration of the study

150   period. The rainfall samples were filtered using 0.2 µm filters at the sampling sites and stored in 2 ml glass vials with screw caps pre-washed several times with the filtered rainwater. The snowfall samples were melted at room temperature, filtered using 0.2 µm filters, and placed in the 2 ml glass vials. To avoid evaporation, all vials were sealed with Parafilm M (Bemis Company, USA, Part no. PM-992) and stored at 4°C.

The samples were analysed using a Picarro Isotopic Water Analyzer (L2120-I) with measurement precision of ±0.6‰ and

155   ±0.2‰ for δD and δ^{18}O, respectively. The sample analysis procedures and quality were certified by the International Atomic Energy Agency (IAEA) through the completion of a round-robin test using samples supplied by IAEA and according to the procedure and criteria outlined in Wassenaar et al. (2021). The error propagation for *d-excess* was calculated according to

Natali et al. (2022) using the error values of ±0.2 ‰ for $\delta^{18}O$ and ±0.6 ‰ for δD and resulting in total uncertainty value of ±2.5 ‰.

160   The samples were injected into the analyzer seven times sequentially, and the first three measurements were discarded to avoid any memory effect from the previous samples. The remaining four measurements were checked for consistency using the criterion of standard deviation not exceeding 1.5‰ and 0.15‰ for δD and $\delta^{18}O$, respectively. The final values were calculated as means of the four valid measurements. If four measurements, satisfying these conditions were not obtained, the samples were re-measured and average of at least three valid measurements was recorded (52 samples). The isotopic ratios were

165   recorded using delta-notation in *per mille* (‰) relative to the Vienna Standard Mean Ocean Water (V-SMOW):

$$\delta = (\frac{R_{sample}}{R_{standard}} - 1) \times 1000‰ \hspace{3cm} (3)$$

where R_{sample} and $R_{standard}$ are the isotope ratios $^2H/^1H$ or $^{18}O/^{16}O$ of the samples and the standard, respectively. Two primary Standard Mean Ocean Water (SMOW) and Standard Light Antarctic Precipitation (SLAP) and two secondary standards were used. The secondary standards were: (i) Tuyuksu Snow Melt Water (TSMW) collected from the Tuyuksu glacier (43.04°N;

170   77.08°E; 3780 m a.s.l.) located in proximity to the UA1 site with δD of –122.0‰ and $\delta^{18}O$ of –17.2‰, and (ii) commercially available Spring Water (SW) with δD of –55.0‰ and $\delta^{18}O$ of –8.5‰.

2.2. Quantifying links between isotopic composition of precipitation, geographical location, and local meteorological conditions

Stepwise regression was used to determine the relationship between isotopic composition of precipitation and latitude,

175   longitude, and elevation. The $\delta^{18}O$ and δD values derived from all event-based samples collected at the individual sampling sites located between 38.56°N – 43.04°N, 68.79°E – 76.99°E, and 486 – 3277 m a.s.l. (Table 1) were the response variables.

The effects of surface air temperature and precipitation depth on mean monthly values of $\delta^{18}O$ and δD were examined using linear regression and the method of Dansgaard (1964). The latter suggested that a difference between isotopic ratios of $\delta^{18}O$ averaged over warm (May – October) and cold (November – April) periods are indicative of the control by either by local

180   temperature or precipitation amount over isotopic ratios. Positive values of the $\delta^{18}O$ difference are typical of the high- and mid-latitude continental regions and indicate a strong surface air temperature control over the isotopic composition of precipitation.

2.3 Local Meteoric Water Line (LMWL)

There are two approaches to defining LMWL. The first approach assigns equal weighting to all data points regardless of the

185   amount of precipitation they represent and is used to evaluate the atmospheric and hydrometeorological processes controlling the isotopic composition of precipitation. However, samples obtained from smaller precipitation events tend to have lower *d-excess* due to the sub-cloud evaporation leading to sample enrichment in comparison to samples obtained from the heavy precipitation events which are more depleted (Hughes and Crawford, 2012; Crawford et al., 2014). To overcome this problem and to represent hydrologically significant precipitation, which is important for local hydrological applications, weighted

190   precipitation is used. This method requires data on precipitation depth (Table 1). Both approaches were used for comparison and to produce recommendations on the LMWL development in the study region considering that precipitation depth may not be available in other projects.

Ordinary Least Squares Regression (OLSR) was used to define LMWL from the unweighted samples (n=915; Table 1). Precipitation depth was recorded for 874 samples (Table 1) which were used in the precipitation-weighted analysis. Six

195   regression methods were applied to the event-based precipitation samples: three non-weighted (OLSR, Reduced Major Axis Regression (RMA), and major axis regression (MA)) and three precipitation-weighted (Precipitation-Weighted Least Squares

Regression (PWLSR), Precipitation-Weighted Reduced Major Axis Regression (PWRMA), and Precipitation-Weighted Major Axis Regression (PWMA)) (Hughes and Crawford, 2012; Crawford et al., 2014). The Local Meteoric Water Line Freeware (available at http://openscience.ansto.gov.au/collection/879) was used in all calculations. The software calculates the following parameters: slope of regression line (a), standard deviation of the slope (sa), intercept of regression line (b), standard deviation of the intercept (sb), average value of the sum of the squared errors of three methods, either OLSR, RMA and MA or three precipitation-weighted regressions, root mean Sum of Squared Errors (RMSSE), which allow inter-comparison of different regression methods. The proximity of the RMSSE values to 1.0 was used as an indicator of the method suitability for the analysed data set. The t-test was applied to evaluate statistical significance of a difference between OLSR and each other regression method.

2.4 Back trajectory modelling and cluster analysis using HYSPLIT

Isotopic composition of precipitation is determined by the combination of the origin of moisture, history of atmospheric water transport, and local conditions (Rozanski et al., 2013). To evaluate the controls of atmospheric circulation over the isotopic composition of precipitation and characterise its geographical sources, $\delta^{18}O$, δD, and *d-excess* values were used in conjunction with the three-dimensional atmospheric back trajectory analysis. The HYbrid Single-Particle Lagrangian Integrated Trajectory (HYSPLIT) model (version 5.2.0) with the Global Data Assimilation System (GDAS) meteorological input (Draxler and Rolph, 2013; Stein et al., 2015; Rolph et al., 2017). HYSPLIT, which has a horizontal resolution of 1°, was run for each precipitation event registered at UA1, CKS2, AA1, and CHK1 (Table 1) using latitude, longitude, and elevation of the sites as input parameters. All sites were located between 1255 and 2571 m a.s.l. The use of site elevation as starting point is justified because in the region, most moisture in the air column is contained between 1500 and 3000 m where lifting condensation level is positioned and where precipitation forms (Chen et al., 2024; Zongxing et al., 2016). The length of integration was 120 hours because uncertainty in the calculation of trajectories increases with time afterwards (Draxler and Rolph, 2013). The global median value of water vapour residence time in the atmosphere is estimated as approximately five days (120 hours) although several studies estimate it as 8 - 10 days (Van Der Ent and Tuinenburg, 2017).

In line with previous studies (Jorba et al., 2004; Wu et al., 2015; Pérez et al., 2015; Bagheri et al., 2019; Kostrova et al., 2020) and to comply with the HYSPLIT cluster analysis function requirements, single trajectories were calculated instead of trajectory ensembles, potentially introducing uncertainty. The starting time of each back trajectory was defined as the hour closest to the start of precipitation event. The median duration of precipitation events was 240 minutes. A comparison between trajectories calculated for the start and the end of precipitation events exceeding 660 minutes (90th percentile) was performed. The differences between the coordinates of their point of origin was within the HYSPLIT resolution.

The generated back trajectories were grouped using cluster analysis based on minimizing distance and maximizing difference between clusters with distinct trajectories (Dorling et al., 1992). The HYSPLIT 5.2.0 built-in cluster analysis function (available at https://www.ready.noaa.gov/HYSPLIT_hytrial.php) was used to derive clusters for the UA1, CKS2, AA1 and CHK1 sites. Total spatial variance (TSV), defined as sum of the spatial variances of all clusters, was used to determine the optimal number of clusters. The percentage of change in TSV was plotted against the number of clusters and the first large increase in the change of TSV was taken as an indicator of the final number of clusters (Wilks, 1995; Kostova et al., 2020).

Isotopic ratios and *d-excess* values were initially analysed for the clusters generated for each site and season. However, many trajectory clusters generated for different sites were similar (e.g., the 'West' cluster was generated for each site; see Figure 6 further in the text). Splitting the data by season for each site resulted in a small number of members in each cluster. To overcome this problem, similar trajectory clusters from different sites were merged. Some of the clusters included data from all sites (e.g. West) while others were limited to a smaller number of sites. Isotopic ratios and *d-excess* were averaged by

cluster and meteorological seasons. Analysis of variance (ANOVA) and pairwise t-tests were used to test whether the differences between δ^{18}O, δD, and *d-excess* values attributed to different clusters were significant at 95% confidence level.

2.5 Quantifying relative contributions of the trajectory sources to total precipitation.

240 The proportional contributions of the trajectory sources to the total precipitation were quantified using a linear mixing model whereby two isotopic signatures (δ^{18}O and δD) enable partitioning of the total precipitation between three sources (Phillips and Gregg, 2001). Fractional contributions were calculated using Equations (4) and (5) (Phillips and Gregg, 2001):

$$\delta_P = f_A \delta_A + f_B \delta_B + f_C \delta_C \tag{4}$$

$$f_A + f_B + f_C = 1 \tag{5}$$

245 where f_A, f_B and f_C are fractional contributions of different trajectory groups to local precipitation, δ_A, δ_B, δ_C are isotopic values of each group by season, and δ_P is seasonal mean isotopic value for all precipitation events during the sampling period. The software *IsoError Version 1.04* (available at http://www.epa.gov/eco-research) (Phillips and Gregg, 2001)) was used to apply the mixing model.

The mixing model was limited to a maximum of three contributing trajectory sources (Equations 4 - 5) but up to five clusters

250 of back trajectories were identified. The number of clusters was reduced to form three trajectory groups for different seasons using the following criteria: (i) direction of travel; (ii) distance travelled; and (iii) whether local circulation trajectories remained within the catchment boundaries. Clusters 1, 2 and 3 were merged to form a single (West) group because, despite the differences in directions, they were associated with the long-distance transport along the peripheries of depressions originating over the Atlantic. Statistical significance of differences between δ^{18}O, δD, and *d-excess* values associated with

255 different groups were assessed using ANOVA.

3 Results

3.1 Seasonal and spatial variability in δD and δ^{18}O.

The descriptive statistics of δD and δ^{18}O derived from the event-based precipitation at each catchment are summarized in Figure 2 and Table S1 (where data are shown for each sampling site and for three types of precipitation: snow, rain and mixed).

260 The δ^{18}O and δD means and standard deviations for all events between 2019 and 2021 were -8.6±6.5‰ and -56.1±50.1‰, respectively. Rain samples (n=528) were characterized by the higher mean δ^{18}O and δD values of –4.9‰, and –28.1‰, respectively, whereas snow samples (n=260) have lower mean δ^{18}O and δD values of −15.4‰ and −110.7‰, respectively (Table S1). Variability in the snow sub-set was higher than in the rain sub-set with standard deviations of ±5.5‰ (δ^{18}O) and ±44.6‰ (δD) for snow and ±4.3 ‰ (δ^{18}O) and ±30.0‰ (δD) for rain. The mixed precipitation data set, based on 120 samples,

265 showed intermediate values of δ^{18}O of −9.7‰ and δD of −61.7‰. Contrary to the expectation that standard deviations of the mixed precipitation isotopic ratios should be the highest, reflecting different proportions of solid and liquid content of precipitation in a sample, their values were the lowest for δ^{18}O and broadly the same as for rain for δD (Table S1).

Clear seasonal cycles were observed in δD and δ^{18}O values in each catchment where isotopic ratios were higher in summer and lower in winter (Fig. 2a, b; Table S1). In the event-based precipitation samples, δ^{18}O and δD values varied widely from

270 −33.6 to 8.6‰ and from –258.8 to 45.2‰, respectively (Fig. 2a, b). Both δ^{18}O and δD showed larger variability in those months when snow and mixed precipitation were observed, namely between November and March in more southerly CHK catchment and in April-May and November in other catchments (Fig.2a, b; Table S1). The CHK3 site (17% of all CHK samples; two samples only in JJA) was located at 486 m a.s.l. enhancing the difference with other catchments and sites (Fig.

3). Between late spring and early autumn, the between-sample variability was reduced, and the standard deviations were lower
except for the higher-elevation and more northerly catchments, i.e. UA and AA (Fig. 2a, b).
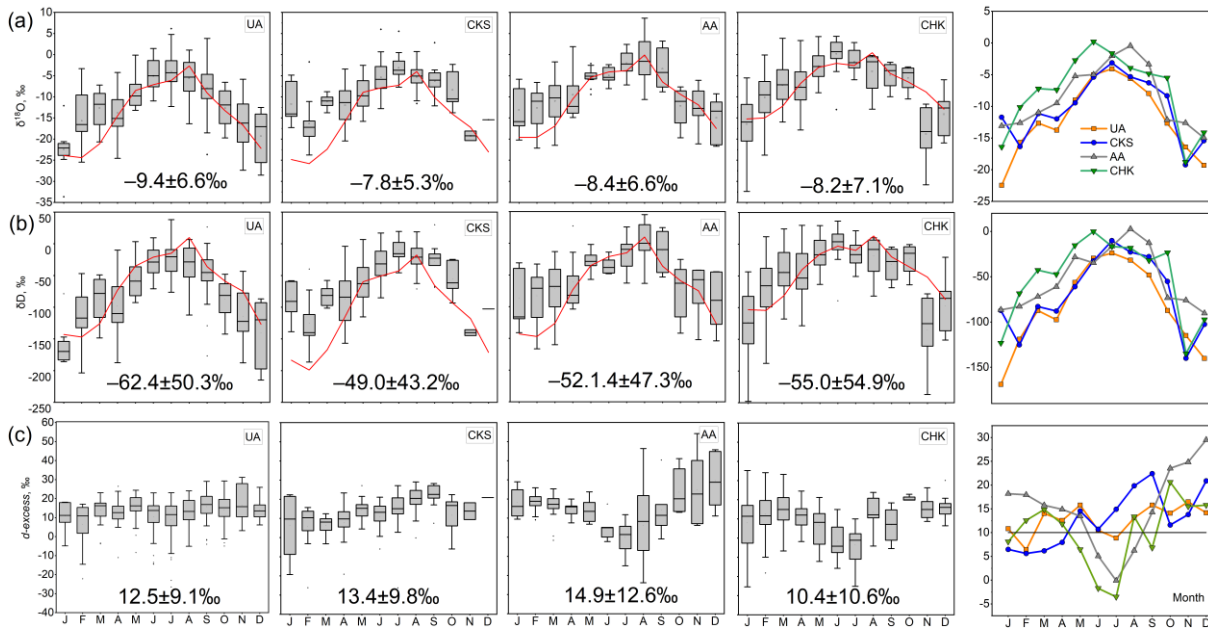
Figure 2: Boxplots of (a) δ^{18}O, (b) δD, and (c) *d-excess* in precipitation collected at the four catchments (see Fig. 1 and Table 1 for locations of catchments and number of samples) between 2019 and 2021 (left panel) and mean monthly d-excess values (right panel). Precipitation was sampled at three sites in CHK and CKS and data from all sites are included. Annual mean values ± standard deviation calculated for the 2019 – 2021 period are shown. The horizontal line in (c; right panel) shows the global mean *d-excess* (10‰). The red line shows data from the Waterisotopes Database (Bowen, 2022). The Waterisotopes Database data were averaged over all sampling locations in CKS and CHK.

The relationship between isotopic precipitation composition and latitude, longitude and elevation were quantified by the following equations, derived using all available samples:

$$\delta^{18}O = 36.3 - 1.18 Lat + 0.07 Lon - 0.00001 E \tag{6}$$

$$\delta D = 342 - 10.75 Lat + 0.73 Lon - 0.002 E \tag{7}$$

where Lat is latitude (⁰), Lon is longitude (⁰), and E is elevation (m a.s.l.). Regression equations for four meteorological seasons are shown in Table S2. Latitude is the only statistically significant predictor of both δ^{18}O and δD in the overall data set ($p < 0.01$) while relationships with longitude and elevation were not statistically significant. Elevation was the only significant predictor of δ^{18}O and δD in winter. Elevation and longitude were significant predictors in autumn ($p < 0.05$).

Three sites with an elevation difference of more than 800 m a.s.l. in CHK and CKS allowed examination of elevation gradients in isotopic ratios and *d-excess* which were calculated using the lowest and the highest sampling points for which data were available (Table 1). For both δ^{18}O and δD, the gradients were highest in summer but not consistent between CKS and CHK (Fig. 3). Very few samples were available for the CHK3 (city of Tashkent) site located in the foothills and isotopic ratios were not consistent with the high temperatures registered at this site.

The indices, derived from the application of Dansgaard (1964) method confirmed the links between isotopic ratios and temperature evident from Figure 2. The indices were positive, ranging between 7.0‰ in CKS and 8.6‰ in UA (Table S3)

therefore demonstrating a strong temperature effect and lesser influence of precipitation amount on isotopic ratios. For the whole data set, coefficients of determination for the event-based values of δD and δ18O and air temperature (measured at the sampling sites) were 0.56 and 0.54, respectively (Equations 8 – 9) ranging between 0.46 and 0.66 for the individual sampling sites (Table S4). They were statistically significant at the 95% confidence level except CHK3. The δ18O and δD changed by 0.62‰ and 4.68‰ per one degree temperature, respectively, for the whole data set. The highest coefficients were obtained for the AA1 and CHK1 sites (0.66 and 0.64, respectively) and the lowest (0.27) for CHK3. The highest gradients were observed at CHK1 (0.74‰ and 5.50% per 1°C) and the lowest at CHK3 (0.32‰ and 2.46% per 1°C) (Table S4).

$$\delta^{18}O = 0.62t - 10.61, \ R^2 = 0.56 \tag{8}$$

$$\delta D = 4.68t - 71.64, \ R^2 = 0.54 \tag{9}$$

where *t* is air temperature (°C) at the sampling sites.

There was no statistically significant correlation between isotopic ratios and precipitation depth in the study region.

3.2 *d-excess* variations over the region and elevation effects

The mean seasonal *d-excess* values ranged between 13.07‰ and 15.15‰ in SON, DJF and MAM. In JJA, the mean *d-excess* value was 12.41±10.26‰ (Figure 2c). In the AA and CHK catchments, minimum *d-excess* values were observed in June-July (when mean monthly values were negative) increasing in DJF (AA), and MAM and SON (CHK). In UA and CKS, seasonal cycles were less pronounced (UA) or different, with a maximum in August – September (CKS). In CKS, located on the shores of Lake Issyk Kul, *d-excess* was below 10‰ between January and April.

In spring, *d-excess* values above 10‰ were observed in all catchments (except CKS in March – April) and autumn – early winter in line with the occurrence of the wet season (Fig. 1). In the AA catchment, values over 10‰ were observed between September and May. Values more than 20‰, indicating strong re-evaporation, were evident between October and December in the AA catchment and in the individual months in the same period in CHK (October) and CKS (September, December). The particularly high mean monthly value reaching 29.5‰ was recorded in the AA catchment in December although this calculation is based on seven samples (Table S1).
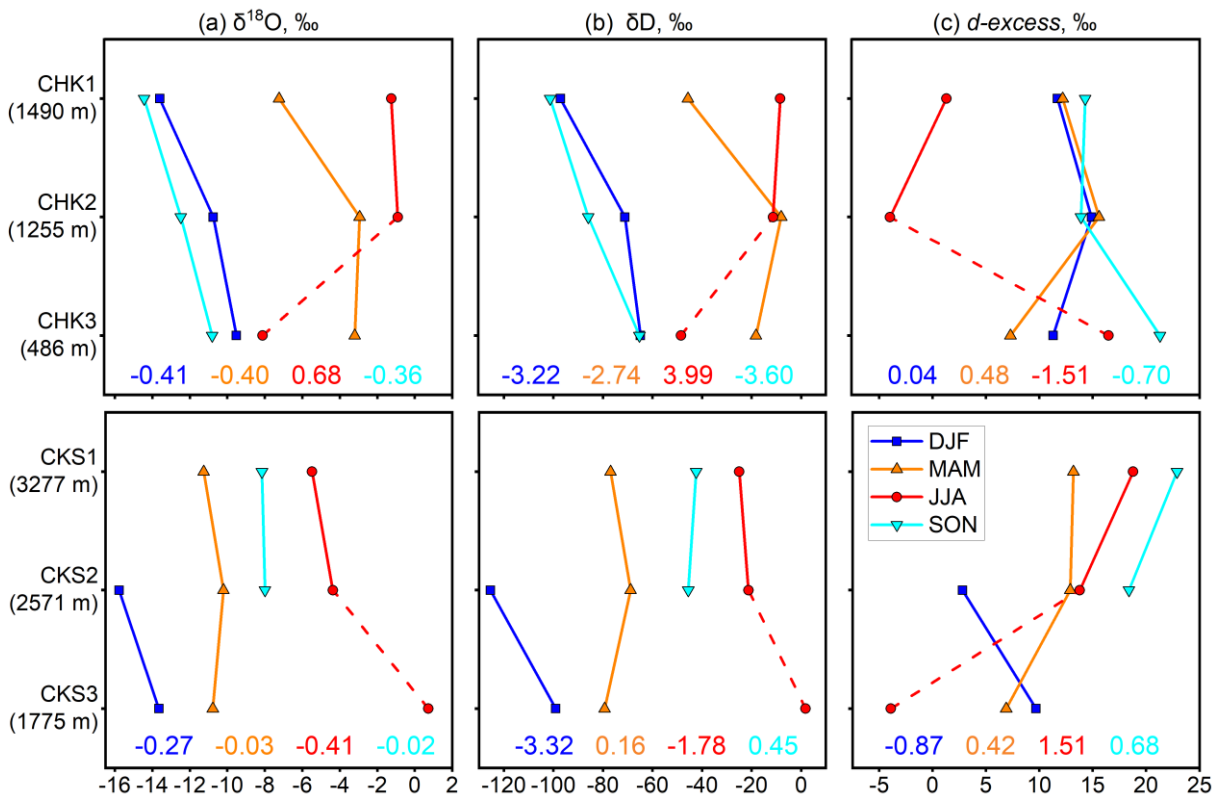
Figure 3: Changes with elevation in (a) δ¹⁸O, (b) δD, and (c) *d*-excess by season in CHK (upper panel) and CKS (bottom panel). Dashed lines indicate small number of samples and low precipitation per event in CHK3 and CKS3. Numbers show seasonal values of elevational gradients (‰ per 100 m).

Figure 3 shows elevational profiles of *d-excess*. In CKS, *d-excess* values increased with elevation from –3.9‰ (n=3) at CKS3 located at 1755 m a.s.l. to 18.9‰ (n=28) at the CKS1 (3277 m a.s.l.) in JJA. Similar altitudinal profiles were observed in MAM albeit with a reduced gradient (6.9‰ and 13.2‰ at CKS3 and CKS1, respectively) and in SON when data were available for the CKS2 (2571 m a.s.l.) and CKS1 sites only (Fig. 3c). In CHK, *d-excess* values changed little at the higher-elevation sites of CHK2 (1255 m a.s.l.) and CHK1 (1490 m a.s.l.) in DJF, MAM, and SON (between both, seasons and sites). The largest seasonal variations occurred at the low-elevation (486 m a.s.l.) CHK3. The steepest elevational gradients were observed in JJA when the mean seasonal *d-excess* declined from 16.5‰ (n=2) in CHK3 to a negative value of -3.9‰ (n=4) in CHK2. This trend was opposite to CKS. Similar but less pronounced gradients were observed in SON. The high *d-excess* values at CHK3 were not consistent with its low elevation, high air temperature observed during the considered precipitation events (29.8°C) (Table S3), and small precipitation depth (on average, 0.1 mm per event).

Analysis of the overall event-based data set showed that there were no significant geographical controls over *d-excess*. However, analysis of the seasonal sub-sets showed that elevation was a significant predictor of *d-excess* (p < 0.01) in all seasons. Longitude was statistically significant predictor of *d-excess* in MAM (p < 0.05) and SON (p < 0.05) (Table S2).

3.3 LMWL for the mountains of Central Asia

LMWLs were calculated using the whole data set and for the individual catchments (Tables S5-9). The LMWL developed from the whole set of the event-based precipitation samples (Table 1; Fig. 4a) using the most common unweighted OLSR method (Section 2.3) was:

$$\delta D = (7.56 \pm 0.05)\delta^{18}O + (8.65 \pm 0.54), \ R^2 = 0.96 \tag{10}$$

The LMWL developed from 149 mean monthly values including the Dushanbe monthly cumulative precipitation samples (Fig. 4b) using the same regression method was:

$$\delta D = (7.6 \pm 0.1)\delta^{18}O + (9.6 \pm 1.2), \ R^2 = 0.97 \tag{11}$$

350 Figure 4 and Table S5 show the parameters of the derived regression equations. The slope and intercept values were lower (Equations 10-11; Fig. 4a-c) than those of the GMWL (Dansgaard, 1964). The 95% confidence intervals in Equation 10 were $7.6 - 9.7$ for the intercept and for $7.5 - 7.7$ for slope, respectively. the respective confidence intervals in the Equation 11 were $7.2 - 11.9$ and $7.3 - 7.8$. For the total study area, the slope changed from 6.1 ± 0.1 in JJA to 8.1 ± 0.1 in DJF and intercept 2.7 ± 0.7 in JJA to 13.8 ± 2.1 in DJF. The DJF slope and intercept values in OLRS LWML, derived from 17 event-based samples, were

355 lower in CKS than in other catchments at 6.7 ± 0.5 and -12.1 ± 8.3, respectively (Fig. 4d). The slope value for DJF was close to that in JJA (in contrast to other catchments) indicating strong evaporation from the lake.
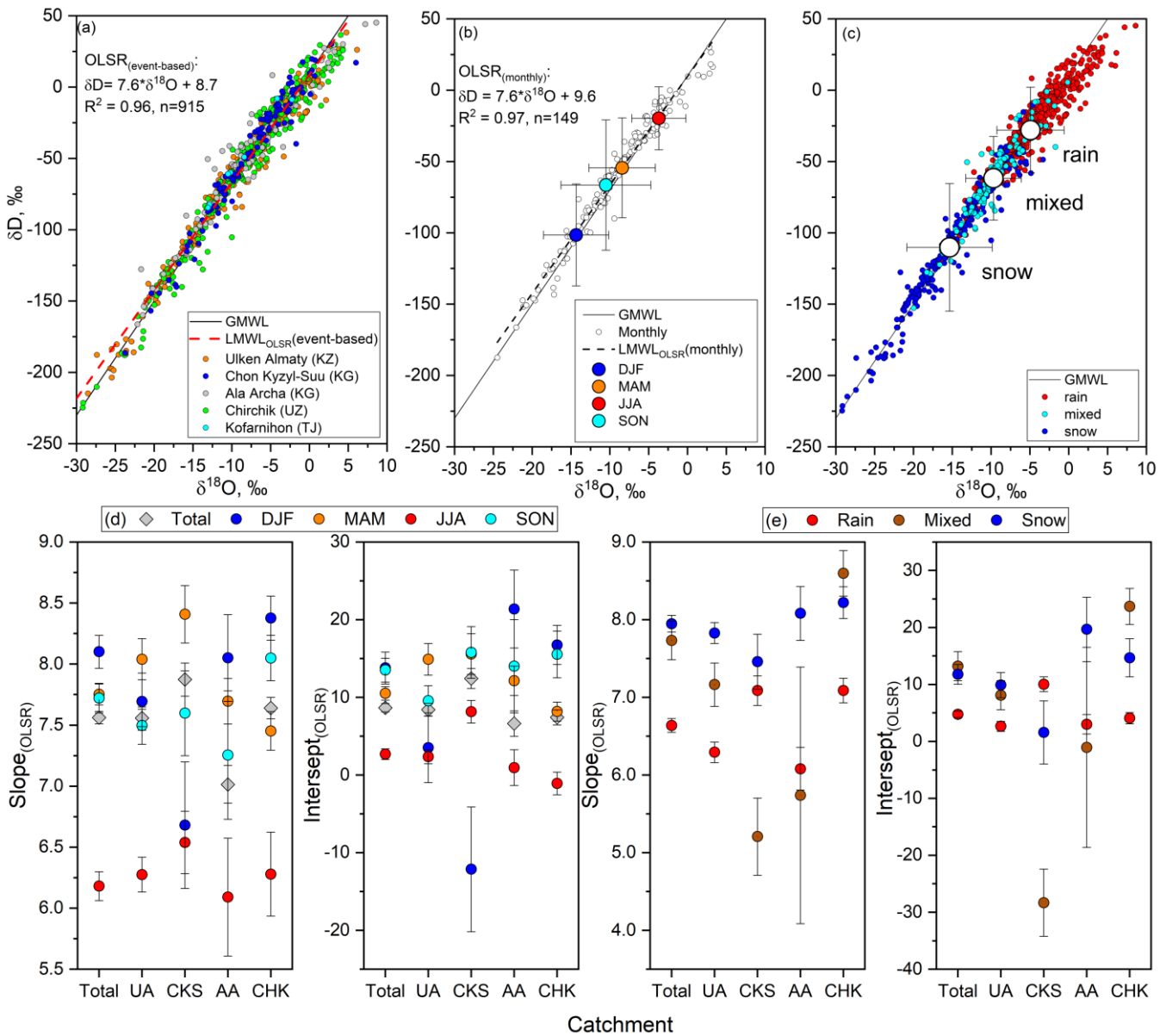
Figure 4: The upper panel shows dual δD and $\delta^{18}O$ plots for (a) the event-based samples for individual catchments, (b) monthly

360 averaged values and seasonal means, and (c) different types of precipitation. The lower panel shows the OLSR-based LMWL slopes and intercepts using (d) event-based data for each catchment by season and (e) by type of precipitation.
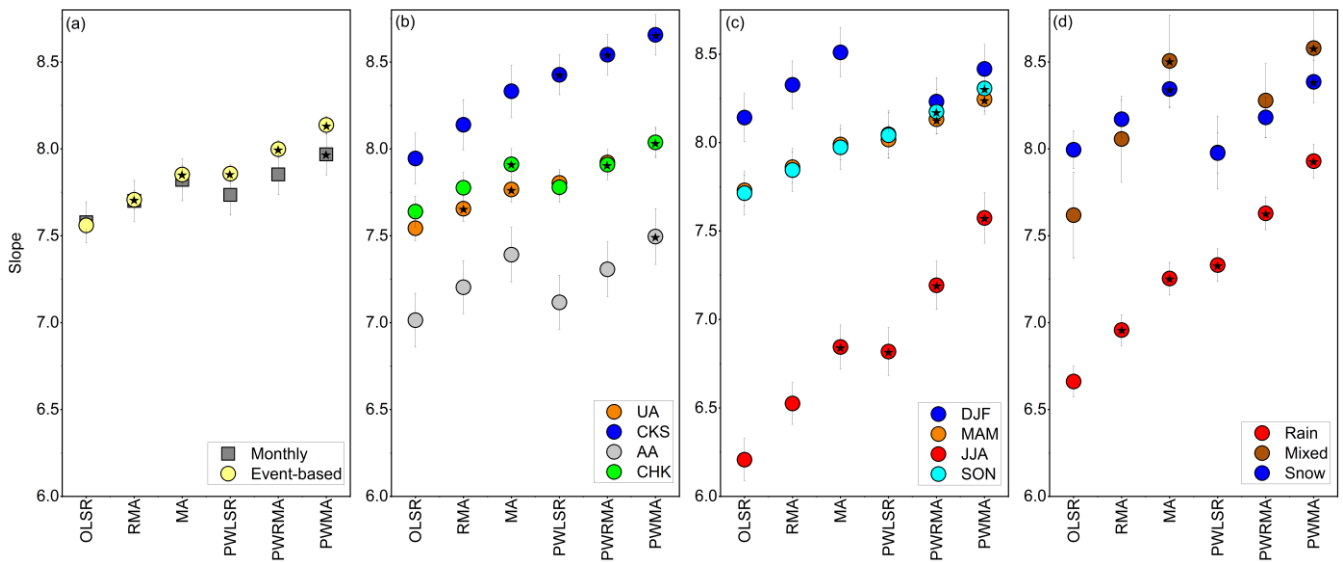
Figure 5: LMWL slopes derived from the regression equations developed using six methods (see Section 2.3 for abbreviations) for (a) event-based and monthly data set for all samples across the region, (b) by catchment, (c) by season, and (d) by precipitation type for the event-based samples. Statistically significant values are marked with a star sign. The values of slopes and intercepts and the outcomes of t-test of between-method differences are presented in Tables S5-S9.

The performance of different regression methods was assessed using the RMSSEav statistics (Section 2.3). For all six methods, RMSSEav values were close to 1 indicating good performance, however, the best regression fit was obtained by the RMA and PWLSR methods for the non-weighted and weighted precipitation, respectively (Table S6-S9). Generally, the weighted methods (PWLSR, PWRMA, and PWMA) generated steeper LMWL slopes than the non-weighted methods (OLSR, RMA, and MA). However, t-test, applied to assess the differences between the regression metrics generated by the six methods and OLSR, showed that results of the RMA method were not significantly different from OLSR (p > 0.05) when calculations were made for individual basins, seasons, and types of precipitation with two exceptions: (i) event-based rain only sub-set and (ii) all event-based samples combined across the region (Tables S5, S9). Parameters of the regression equations for each catchment, season, and precipitation type are shown in Tables S5-S9. Here, the outcomes from the OLSR and PWLSR methods are summarised.

For the whole region, the slope values varied from 7.6 (monthly and event-based) OLSR to 7.7 (monthly) and 7.9 (event-based) using PWLSR (Fig. 5a). The performance of the methods varied between catchments (Fig. 5b). The largest between-method differences were observed in CKS (n=149) with slope values ranging between 7.9 (OLSR) and 8.4 (PWLSR). Statistically significant differences between the non-weighted OLSR and the weighted PWLSR method were observed in AA and CHK because of the lower amounts of precipitation, especially in CHK in summer. In the UA and CKS, the differences were not significant. The slope values derived from the event-based precipitation data for SON (n=138) and DJF (n=168) did not vary significantly between the OLSR and PWSLR methods (Fig. 5c) while they were significantly different in MAM (n=273) and JJA (n=290). Larger differences were observed in JJA (n=290) when slope values varied from 6.2 (OLSR) to 6.8 (PWLSR) (Fig. 6c). The similarly large differences characterised the rain sample sub-set (n=514) with slope values ranging from 6.7 (OLSR) to 7.3 (PWLSR) (Fig. 5d).

3.4 Relationships between isotopic composition and precipitation provenance

390   Overall, 766 five-day (120 hours) back trajectories were generated for every precipitation event for four sampling points: UA1 (n=338), CKS2 (n=117), AA1 (n=115), and CHK1 (n=196) (Table 1). Overall, five clusters were identified: northern part of Kazakhstan – southern Siberia (North - Cluster 1), south-eastern Europe, Black Sea and Caspian Sea (West - Cluster 2), Iran and eastern Mediterranean (South-West - Cluster 3), lower reaches of the Syr Darya and Amy Darya and irrigated area around the Aral Sea (Aral - Cluster 4), and precipitation formed within the study catchments (Local - Cluster 5).

395   Clusters 1 and 2 were identified at each site accounting for 6-26% and 5-19% of all trajectories (Table 2; Fig. 7). The Cluster 1 trajectories were most frequent at UA1 and least frequent at CHK1 and were the most frequent group in JJA overall. In DJF, the Cluster 1 trajectories were registered only one and eight times at UA1 and CHK2 (Fig. 7). The Cluster 2 trajectories were most frequent at CHK1, and least frequent at UA1 (observed three times per season in MAM, JJA and SON) and CKS2 (observed twice per season in DJF, JJA and SON). The Cluster 3 trajectories originated in Iran reaching UA1 and AA1

400   predominantly in DJF and MAM but they were not observed at CHK1 and CKS2 (Fig. 7). While limiting trajectories to 120-hour duration places their origin in Iran, the extension of their duration leads to the eastern Mediterranean albeit with higher uncertainty. Clusters 1, 2 and 3 represented the long-distance moisture transport with the mean trajectory lengths and standard deviations of 1738±451, 3285±1109 and 2652±185 km, respectively. Trajectories from Clusters 1, 2 and 3 represented circulation along the peripheries of the low-pressure systems located north-west or west of the study region, and the differences

405   between them were due to the latitudinal positions of the low-pressure system centres. Cluster 4 included shorter trajectories (1188±237 km) to UA1 and CKS2 from the irrigated lands located along the Syr Darya and Amu Darya rivers, and the Aral Sea. This cluster accounted for 33% and 44% of all trajectories at UA1 and CKS2, respectively (Table 2; Fig. 6), with the highest frequency in MAM and JJA (Fig. 7). The lengths of the 5-day trajectories in Cluster 5, representing precipitation formed locally, varied between 292 km at CKS2 to 565 km at AA1 with a mean length of 438±140 km. There is uncertainty

410   about allocating trajectories to Clusters 4 and 5 at CHK1 because, although the Cluster 5 trajectories satisfied the allocation criteria, the lower part of the CHK catchment is irrigated and the Chirchik is a tributary of the Amu Darya. Trajectories of this cluster were observed at each site accounting for 26% (UA1) to 45-61% (other sites) of all trajectories (Table 2).
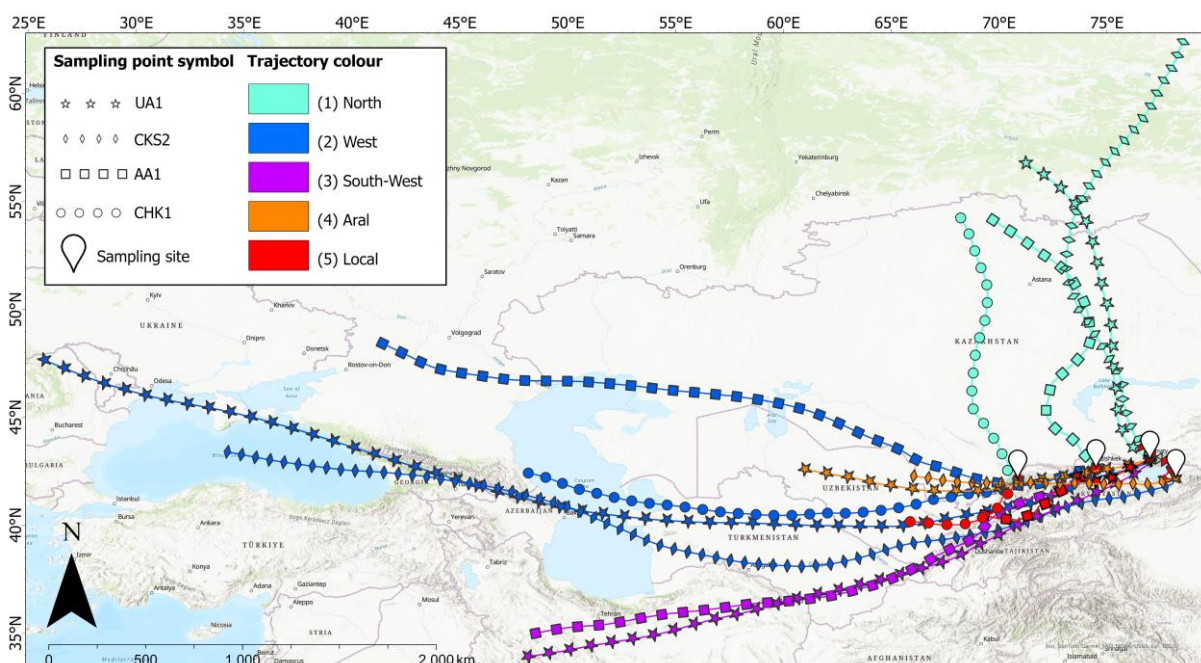
415

Figure 6: Trajectory clusters including mean back trajectories (as generated by HYSPLIT) for the original clusters for four sampling sites for the study period. ESRI ArcGIS Pro Word Topographic Map and World Hillshade are used as background.

420 Isotopic ratios and *d-excess* values averaged over the trajectory clusters by site are shown in Table 2; the box plots are shown in Figures S2 and S3. The between-cluster differences in $\delta^{18}O$ were largest in JJA and DJF, while in MAM and SON (wet seasons; Fig. 1c), they were not statistically significant at 95% confidence level (Fig. 7). In DJF, isotopic ratios of Cluster 1 precipitation were less negative with the mean $\delta^{18}O$ value of -12.01‰ while ratios associated with Cluster 2, representing the most long-distance transport from the west, were more negative with the mean $\delta^{18}O$ of -18.29‰ (Fig. 7a). However, the less

425 negative values of $\delta^{18}O$ and δD were observed at AA1 in Cluster 2 (−6.4 ‰ and −35.0‰, respectively) whereby trajectories started over the East European Plain and crossed the deserts of western Kazakhstan. In JJA, the highest mean $\delta^{18}O$ value of 0.01‰ characterised with Cluster 2. The lowest mean $\delta^{18}O$ values characterised Cluster 3 in both JJA and SON (−6.94‰ and −17.6‰, respectively). Cluster 5 was characterised by the highest in-cluster variability in $\delta^{18}O$. At UA1, AA1, and CHK2, Cluster 5 trajectories arrived predominantly from the south-west and corresponded to more negative isotopic values while at

430 CKS2, they arrived from the north-east and corresponded to the higher isotopic ratios (Fig.6; Table 2).

The between-cluster differences in *d-excess* were significant in all seasons except SON (Fig. 7b). In DJF, the lowest mean *d-excess* value (5.7‰) characterised Cluster 2 and highest (18.6‰) – Cluster 1 (Fig. 7b). The highest mean JJA value of 17.2‰ characterised Cluster 3 arriving from Iran to UA1 and AA1. Cluster 4 trajectories originating over the irrigated lands in the Aral Sea basin had the mean annual *d-excess* of 14.4‰ and 13.9‰ at UA1 and CKS2 (Table 2). Cluster 5 was characterised

435 by the highest variability in *d-excess* values (Fig. 7b).
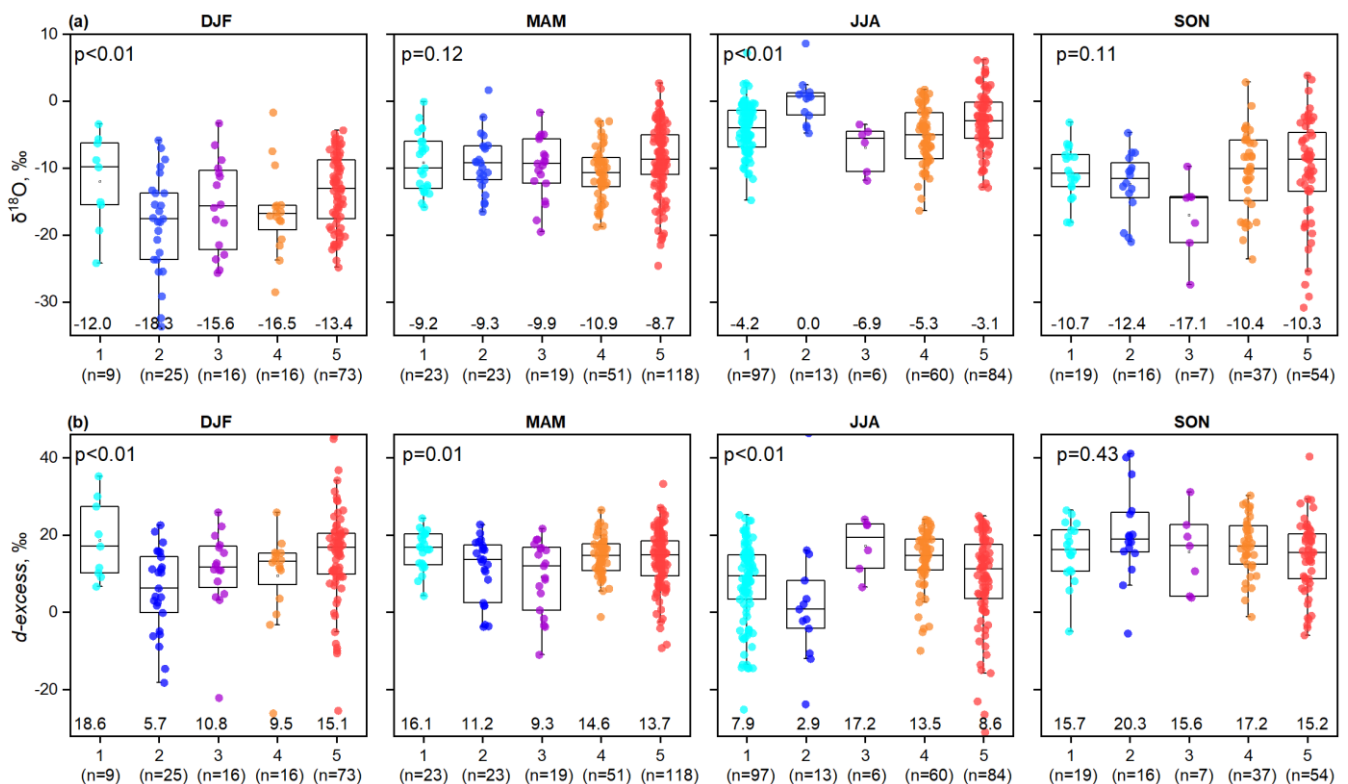
Figure 7: Seasonal values of (a) $\delta^{18}O$ and (b) *d-excess* according to the trajectory clusters. Numbers along the X-axes show the number of events in each group and season.

440 Table 2: Frequency of trajectories by cluster and mean values (upper line) and standard deviation (lower line) of δ18O, δD and *d-excess* (‰). C is cluster; SD is standard deviation; N is number of trajectories corresponding to individual precipitation events and their proportion of the total for each site; Lat is latitude (ºN), Lon is longitude (ºE); D is distance from trajectory source (120 hour iteration) to the sampling point (km). Seasonal mean temperature and total and mean precipitation were derived for the days when precipitation samples were collected over the sampling period (Table 1) and averaged (summed) 445 over trajectory clusters and seasons.

C	δ18O	δD	*d-excess*	Lat	Lon	N (%)	D	Seasonal mean t, ºC				Seasonal mean P, mm/event				Seasonal total P, mm			
	Mean (upper line) / SD (lower line)							DJF	MAM	JJA	SON	DJF	MAM	JJA	SON	DJF	MAM	JJA	SON
UA1																			
1	-6.9	-43.9	11.7	56.46	70.83	88	1625	-10.4	-2.1	7.3	-0.8	2.0	10.7	4.6	4.9	2	85	277	88
	4.4	31.2	8.6	6.41	9.27	(26)													
2	-15.9	-120.0	6.8	46.49	25.75	17	4452	-13	-6.1	10.8	2.1	4.4	5.8	2.3	6.0	35	17	5	6
	9.9	77.5	10.8	12	7.16	(5)													
3	-13.5	-98.1	10.1	33.59	48.51	31	2782	-10.2	0.0	5.6	-8	2.3	6.9	11.5	3.3	23	69	69	17
	7.1	56.0	10.8	5.93	8.78	(9)													
4	-9.8	-63.9	14.4	42.4	61.06	113	1355	-9.5	-0.2	7.3	-1.3	4.1	5.2	6.3	4.2	45	194	252	104
	6.1	46.2	6.9	5.48	6.48	(33)													
5	-8.5	-55.3	12.9	42.1	73.29	89	345	-9.6	-0.6	7.8	0.6	3.6	7.0	4.8	3.3	22	169	148	85
	6.6	48.5	10.4	2.57	6.86	(26)													
CKS2																			
1	-7.7	-41.8	19.8	61.32	77.2	7	2403	-	0.6	9.1	-	-	5.2	14.1	-	-	16	56	-
	4.1	36.0	4.9	7.08	20.16	(6)													
2	-12.5	-83.8	16.2	44.68	31.4	6	3910	-4.2	-	10.4	-6.8	8.9	-	7.3	10.7	18	-	15	21
	7.7	62.0	3.5	6.33	25.5	(5)													
4	-8.1	-51.0	13.9	42.57	66.33	51	1020	-3.6	2.4	9.6	5.8	3.4	7.6	5.8	6.8	17	99	117	74
	5.5	46.7	9.1	4.71	6.68	(44)													
5	-6.3	-38.6	12.0	43.89	75.83	53	292	-	6.0	10.4	1.8	-	7.1	5.5	6.5	-	150	148	26
	4.9	37.0	10.0	3.21	3.72	(45)													
AA1																			
1	-5.2	-31.7	9.5	53.71	70.3	14	1497	-	2.4	17.4	3.9	-	7.2	3.8	5.4	-	43	27	5
	6.1	39.8	3.5	6.55	10.14	(12)													
2	-6.4	-35.0	15.9	47.09	41.76	17	2798	-5.7	-1.2	17.6	2.6	7.4	6.2	2.9	5.2	15	12	17	36
	6.8	44.8	4.6	7.67	18.62	(15)													
3	-10.6	-70.0	14.6	34.81	48.5	17	2521	-2.9	4.9	-	-2.4	2.9	4.3	-	10.0	17	39	-	20
	4.9	36.2	1.8	7.41	7.45	(15)													
5	-9.0	-56.2	15.8	40.18	68.91	67	565	-4.7	6.0	13.6	7.4	4.0	6.6	5.3	5.1	88	132	79	51
	6.7	49.9	1.4	3.21	5.52	(58)													
CHK1																			
1	-4.8	-30.7	7.7	54.33	68.29	39	1427	-4.1	0.9	13.2	-	4.5	2.7	5.7	-	36	16	143	-
	5.7	42.1	12.4	6.33	8.94	(20)													
2	-11.3	-82.5	7.5	42.02	48.01	37	1981	-8.3	2.1	15.1	0.0	4.9	5.6	6.2	6.4	59	100	12	32
	7.1	55.7	10.3	8.62	10.65	(19)													
5	-9.4	-63.5	11.8	40.03	65.98	120	549	-4.1	3.0	12.8	-3.4	5.8	6.6	2.3	4.0	263	347	23	48
	7.2	57.7	10.3	3.84	6.53	(61)													

3.5 Relative contributions of moisture sources to precipitation

The three components of the mixing model (Equation 4) were (i) δ_A – precipitation formed inland over the Aral basin (Cluster 4); (ii) δ_B – locally-formed precipitation (Cluster 5); and (iii) δ_C – precipitation associated with the Atlantic depressions (merged Clusters $1-3$) and δ_P was the mean seasonal value of the isotopic ratios (Fig. 8). Using UA1 in DJF as an example, the mean seasonal precipitation isotopic ratios (δ_P) were -134.5 ‰ for δD and -17.9 ‰ for $\delta^{18}O$, respectively. The three components of mixing model isotopic ratios were: δ_A (-121.6 ‰ for δD and -17.1 ‰ for $\delta^{18}O$), δ_B (-91.9 ‰ for δD and -12.7 ‰ for $\delta^{18}O$), and δ_C (-154.3 ‰ for δD and -19.9 ‰ for $\delta^{18}O$). At UA1, three groups of trajectories were registered in each season and at CKS2 $-$ in all seasons except DJF when there was no precipitation associated with local trajectories. Only two groups $-$ local and the westerlies $-$ were represented at AA1 and CHK2.

The proportional contributions of the identified trajectory sources at different sites and seasons are shown in Table 3. The westerly flow was the main contributor to precipitation at UA1 in winter (54%) and at UA1 and CHK2 in summer (49% and 73%, respectively). The Aral basin contributed 46% at UA1 in MAM, and 71.2% and 67.3% at CKS2 in DJF and SON, respectively. In other seasons, the contribution from Aral basin varied between 29% and 37%. Contributions of the locally formed precipitation ranged from 16% to 73% being particularly high at CKS2 in MAM and JJA while the absence of contribution local sources in DJF was likely an artifact of the small number of samples (n=7). Locally formed precipitation prevailed throughout the year at AA1 and at CHK2, except JJA.
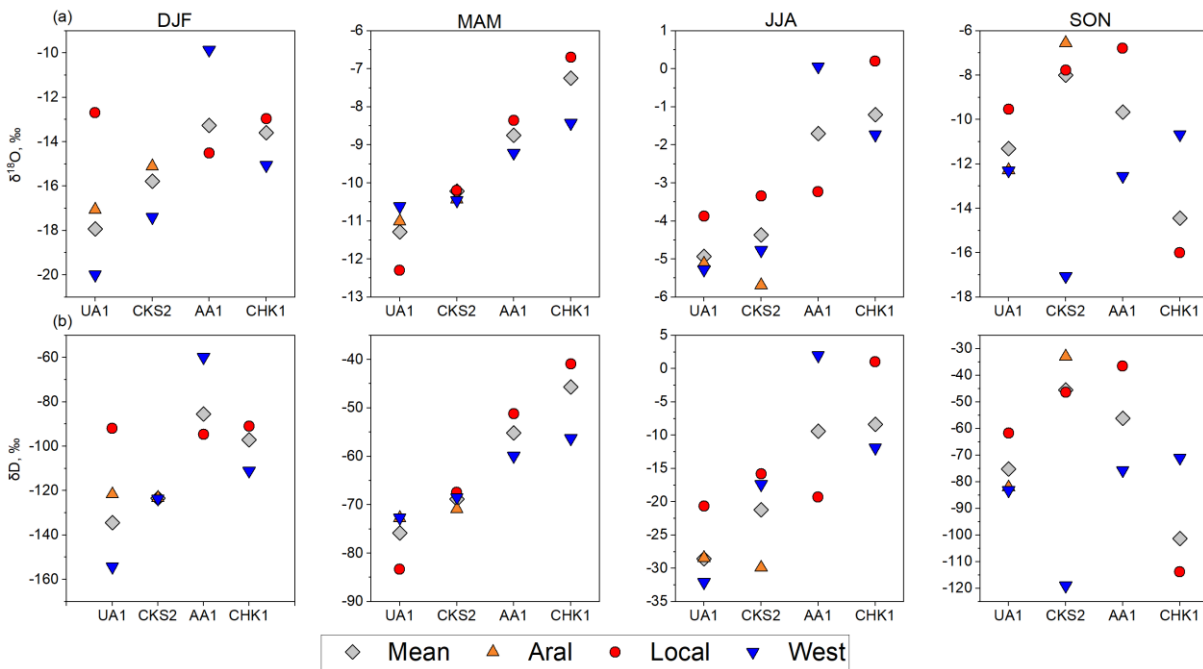
Figure 8: The values of $\delta^{18}O$ (a) and δD (b) characterising seasonal precipitation (δ_P), precipitation originating over the Aral basin (δ_A), locally formed precipitation (δ_B), and precipitation associated with the westerly transport (δ_C) for each basin.

Table 3: Proportional contributions of moisture sources (%) to precipitation and standard errors (SE).

Catchment	Aral				Local				Westerly			
	DJF	MAM	JJA	SON	DJF	MAM	JJA	SON	DJF	MAM	JJA	SON
	Mean (upper line) / SE (lower line)											

UA1	29.1	45.7	29.6	29.5	16.5	29.3	21.6	36.0	54.3	25.0	48.8	34.5
	2.0	3.1	2.1	10.7	1.0	0.6	0.6	0.4	1.0	2.7	1.7	10.4
CKS2	71.2	36.5	37.0	67.3	-	54.3	51.8	21.5	28.8	9.2	11.2	11.2
	1.6	3.4	0.4	5.1		1.9	0.6	5.9	1.6	4.2	0.9	0.8
AA1	-	-	-	-	73.3	54.1	53.6	50.1	26.7	45.9	46.4	49.9
					0.3	1.4	0.4	0.3	0.3	1.4	0.4	0.3
CHK1	-	-	-	-	69.5	68.8	26.9	70.6	30.5	31.2	73.1	29.4
					0.5	0.4	0.4	0.6	0.5	0.4	0.4	0.6

4 Discussion

4.1 Regional trends in isotopic ratios and *d-excess*

Clear seasonal cycles of $\delta^{18}O$ and δD were observed in every catchment with higher $\delta^{18}O$ and δD values registered in summer and lower in winter (Fig. 2) in line with the annual temperature cycle (Fig. 1 b). The maximum enrichment occurred between June in the south (e.g. CHK) and in July−August further north while the most negative values were registered between November and February (Fig. 2; Table S1). In the CKS catchment, the lake effect was evident in the cold season due to the contrast between an enhanced contribution of heavier water vapour from the lake and lighter vapour delivered by the cold air masses (Bowen et al., 2012; Xiao et al., 2017; Minder et al., 2020) resulting in the less negative isotopic ratios of precipitation (Fig. 2). Air temperature was a statistically significant predictor of $\delta^{18}O$ and δD but coefficients of determination of $0.46 − 0.66$ implied that using air temperature as proxy for isotopic signatures may lead to high uncertainty in the reconstructions of isoscapes in the mountains. Similar coefficients were obtained for the Chinese Tien Shan (Wang et al., 2017, 2022), northern Kazakhstan (Yapiyev et al., 2020), and other high- and mid-latitude regions (Gat and Gonfiantini, 1981; Gat, 1996; Rozanski et al., 2013; Putman et al., 2019) although stronger links were reported by Kostrova et al. (2020) for south-eastern Siberia. The $\delta^{18}O$ and δD values changed by 0.62‰ and 4.68‰ per one degree Centigrade, respectively, for the whole data set which is consistent with the results for the Upper Urumchi basin in the Chinese Tien Shan (Pang et al., 2011). Temporal variability in isotopic ratios was stronger in winter and this was also confirmed by the comparison of the snow and rain data sets (Table S1 and Fig. 4). In winter, day-to-day temperature fluctuations, associated with changing synoptic conditions, are stronger than in summer with mean temperature changes between two consecutive days of 4ºC (Shahgedanova, 2002). There was no statistically significant link between isotopic ratios and event precipitation depth even in the arid CHK catchment. Previous studies conducted in the neighbouring regions (Liu et al. 2014; Wang et al., 2018; Juhlke et al., 2019) and globally (Bowen, 2010; Bowen et al., 2019; Putman et al., 2019) also concluded that this correlation was weak.

The observed seasonal cycles of $\delta^{18}O$ and δD were generally consistent with the global interpolation of precipitation isoscapes (Bowen and Revenaugh, 2003; Bowen et al., 2019), the global high-resolution isotope precipitation data (Terzer-Wassmuth et al., 2021), and results reported for the Chinese Tien Shan (Liu et al., 2014; Wang et al., 2019). However, the interpolations significantly underestimated isotopic ratios in the study region between October and March (Fig. 2 a, b) due to the lack of data available to date. For example, the annual mean difference between measured ratios and those derived from the global database (Fig. 2) varied from −0.3‰ (CHK) to 4.8‰ (CKS) for $\delta^{18}O$ and from −6.7‰ (CHK) to 37.4 (CKS) for δD but reached 10.1‰ (CKS) for $\delta^{18}O$ and 52.5‰ (AA) for δD in winter (Fig.2a, b; S1).

In CA, spatial variability in $\delta^{18}O$ and δD in precipitation in all seasons except autumn was characterised by an overall increase in isotopic ratios from north (UA) to south (CHK) (Table S1). The application of stepwise regression to the event-based data (Equations 6 − 7) showed that latitude was a statistically significant predictor of $\delta^{18}O$ and δD in the overall CA dataset. In the

Chinese Tien Shan, mean isotopic ratios, measured at the mountain sites (between 1628 and 2458 m a.s.l. which is similar to the elevations of our sites), were less negative in the south-west and more negative in the north-east in JJA (Wang et al., 2016b). When combined, both data sets confirm this spatial trend with mean JJA $\delta^{18}O$ changing from -1.2‰ and -1.7‰ in CHK1 (70.64°E) and AA1 (74.50°E) to -10.1‰ (93.03°E) and -10.5‰ (94.42°E) in China. In CA, elevation was a significant predictor of $\delta^{18}O$ and δD in winter and autumn and longitude – in autumn and spring, when westerly flow dominates. In the Chinese Tien Shan, there was no clear spatial or elevational trend at the mountain sites in DJF (Wang et al., 2016b). The number of sites in our study was relatively small (Table 1) and CKS experienced the lake effects. Both factors limited the performance of the regression model. Liu et al. (2014) used 29 sampling points in a similar analysis in northern China; Wang et al. (2016b) used 23 sites (although only six were in the mountains). The regression model can be improved in the future using isotopic data from a wider range of geographical locations, e.g. by combining data sets from CA and the Chinese Tien Shan and by including the newly-established sites in the western Pamir where sampling commenced in 2023.

Previous studies in the Chinese Tien Shan and in the western Pamir showed that the annual cycle of *d-excess* was opposite to those of $\delta^{18}O$ and δD with high (positive) values in the cold season and low (negative) values in summer (Pang et al., 2011; Wang et al., 2016b; Zhang and Wang, 2018; Juhlke et al., 2019). The JJA *d-excess* values in AA and CHK, calculated using unweighted precipitation, confirmed this conclusion being as low as -3.5‰ and similar to *d-excess* values measured in Iran and Iraq (Juhlke et al., 2019). Low precipitation amounts and higher temperatures, especially at CHK, enhanced negative *d-excess* values in JJA. There was a clear distinction between the AA and CHK catchments located in the west (72–74.5°E; Table 1) which matched the wider regional pattern, and CKS (78°E) located in proximity to Lake Issyk Kul (Fig. 2c; Table S1) where the lake effect resulted in lower *d-excess* values which fell below 10‰ between January and April increasing to 20-22‰ in August-September (Fig. 2c). The annual *d-excess* cycle in the UA in the north-east of the study area (43°N; 77°E) was less pronounced. This sampling site was located by a much smaller (~ 0.8 km²) mountain lake which freezes in winter. While locations of sampling sites were to an extent defined by the practical aspects of long-term monitoring, the presence of lakes complicated analysis of geographical *d-excess* patterns.

The observed elevational profiles of *d-excess* were inconsistent between sites and seasons (Fig. 3) partly because precipitation events were not always observed on the same days at different sites in the same catchment but also because of the different local conditions. At CKS, *d-excess* increased with elevation in summer in line with the decreasing air temperature and the distance that rain drops travel between the cloud base and land surface (Natali et al., 2022). This is consistent with a broader pattern of elevational change is d-excess described by Bershow (2018). In DJF, when the sub-cloud evaporation effect is absent (Fröhlich et al., 2001), *d-excess* values declined with elevation between the CKS2 and CKS3 sites. Lapse rates of *d-excess* were small in spring and autumn (wet seasons) likely due to the reduced sub-cloud evaporation and the occurrence of predominantly liquid precipitation at lower elevations and snow at CKS1 in spring. Thus, in CKS, *d-excess* values for snow and rain were 9.7‰ and 15.3‰, respectively (Table S1).

In CHK, low-intensity precipitation events dominated in JJA with 86% and 74% precipitation events producing less than 10 mm and 5 mm, respectively. At the same time, air temperatures were high even in the middle mountains, where most samples were collected (Fig. 1; Table 1), leading to a strong sub-cloud evaporation effect. The lowest mean *d-excess* value of –3.9‰ was registered at CHK2 (1255 m a.s.l.) in JJA increasing to an average of 1.3‰ at CHK1 (1490 m a.s.l.), similar to CKS (Fig. 3). However, the mean summer *d-excess* value of 16.5‰ in CHK3 (city of Tashkent, 486 m a.s.l.; derived from two precipitation events only) was inconsistent with the observed meteorological conditions. We suggest that Tashkent, located in the extensively irrigated foothills and featuring urban irrigation, may exhibit higher *d-excess* values in JJA (as well as SON) due to the contribution of water re-evaporated from the irrigated land. Similar oasis effects were reported by Wang et al. (2016a; 2016b) and Zhang and Wang (2018), however, a larger number of samples is required for confirmation.

4.2 LMWL

LMWLs were developed for the study area for the first time to complement those for the Chinese sector of the Tien Shan (Wang et al., 2018). Although, isotopic ratios are controlled by the equilibrium fractionation, in the arid regions, where significant evaporation of precipitation is observed, especially during the events of light precipitation or virga, kinetic
545 fractionation is important resulting in the difference between the GMWL and LMWL (Tian et al., 2007; Wang et al., 2018, 2019; Chen et al., 2021). In CA, the availability of the LMWLs enables quantification of the relative contributions of water sources, including precipitation, to runoff (Bowen et al., 2018; He et al., 2019) and calculation of lake mass balance (Yapiyev et al., 2020). Both tasks are relevant to adaptation policies in this water-deficient region.

Results obtained using monthly and even-based samples were close indicating that either can be used to develop LMWL in
550 the region. Application of the standard OLSR method to the data from individual catchments and seasons showed that higher slope values were observed in winter and spring (7.6 – 8.4) when the air temperature is lower and relative humidity is higher, and when precipitation peaks in spring. The lowest values (6.1 – 6.3) were observed in summer suggesting strong evaporation and a contribution to precipitation from local recycled moisture (Fig. 4; Table S5). The CKS catchment featured strong seasonal variations with the lowest slope value of 6.6 in DJF, pointing at evaporation from the Issyk Kul, and the highest value of 8.4
555 in spring. The seasonal variations in LMWL slope were consistent with those in the Chinese Tien Shan (Wang et al., 2018), however it is difficult to compare spatial variations in the LMWL slopes because of a limited number of sites used in this study. A clear north to south gradient in LMWL slope was reported for the Chinese Tien Shan and adjacent regions with the lowest values observed in the extremely arid Tarim basin (Wang et al., 2018). In our study region, the lowest summer and annual values were observed in AA rather than in CHK catchment although AA is located in the northern part of the study
560 area albeit in the inner Tien Shan.

Previous studies (Hughes and Crowford, 2012; Liu et al., 2014; Wang et al., 2018) demonstrated that low summer precipitation contributes to uncertainty in modelling LMWL. Whilst there was no statistically significant link between isotopic ratios and precipitation depth overall, the potential effects of low-intensity precipitation on summer isotopic ratios especially in the more arid regions warrantied a comparison of different LMWL derivation methods using non-weighted and weighted precipitation.
565 The methods using non-weighted precipitation generated similar results which were not significantly different from the OLSR although the best fit was obtained using RMA method (Table S6-9). The difference between methods based on weighted and non-weighted precipitation were small in all seasons except summer when the largest difference was observed in (i) the AA and CHK catchments and (ii) the rain-only sub-set in all catchments (Fig. 5). The best fit was obtained using PWLSR method (Table S6-9). In the Chinese Tien Shan, similar differences between methods based on weighted and non-weighted
570 precipitation were observed in the southern Tarim basin and the northern Junggar region (Wang et al., 2018). We recommend that the OLSR and RMA methods can be used in the mountains of CA except for the warm season when low rainfall depths are observed under high temperatures when the weighted precipitation the PWLSR method should be used.

4.3 Trajectory sources and *d-excess*

Synoptic-scale patterns of *d-excess* are used to characterise changes in moisture sources but their interpretation is ambiguous
575 especially in CA where water vapour travel large distances (e.g. Cluster 1-3) and is affected by secondary fractionation processes (Bershaw, 2018). In this study, there were well-pronounced differences between the mean *d-excess* values associated with different trajectory sources in all seasons except SON. The highest *d-excess* values in JJA (17.2 ‰; Fig. 7b) were predictably associated with trajectories arriving from Iran extending to the Mediterranean (if the iteration time exceeded 120 hours) in line with the uniquely high *d-excess* values characterising this region (Bershaw, 2018). Trajectories arriving from the
580 Black Sea were by contrast characterised by the lowest mean *d-excess* values in both JJA and DJF (Fig. 7b) because the Black Sea region is characterized by high relative humidity throughout the year. Mean values of *d-excess* associated with Siberian

trajectories cluster varied strongly between the highest in the data set in DJF (18.6±10.3 ‰) and lower values in JJA (7.9±10.6 ‰) in line with seasonal changes in temperature and humidity (Bershaw, 2018; Kostrova et al., 2020). Trajectories originating over the irrigated Aral Sea basin had the mean annual *d-excess* of 14.3±7.6‰ remaining consistently high throughout the year and indicating the contribution of re-evaporated moisture to precipitation.

4.4 Precipitation provenance in Central Asia

The westerly airflow transporting the Atlantic moisture was widely acknowledged as the main source of precipitation in CA based on studies of both climate (e.g. Shahgedanova, 2002) and isotope hydrology (e.g. Tian et al., 2007; Feng et al., 2013). This pathway was detected in all seasons, however, the mixing model results (Table 3; Fig. 8) showed that inland recycled moisture, originating from both the irrigated land in the Aral Sea region and from the study catchments, was the predominant source of precipitation in the study area. This conclusion agrees with Link et al. (2020) who showed that in Kyrgyzstan, the fraction of precipitation that originated from terrestrial sources reaches 61% making it one of the top 10 countries with the highest contributions from local terrestrial sources. Precipitation maxima in all catchments occur in MAM except UA where it peaks in May-July (Fig. 1). In MAM, precipitation associated with the local trajectories accounted for 52-54% in CKS and AA increasing to 69% in CHK. The Aral Sea region contributed 46% and 37% in UA and CKS, respectively (Table 3). Precipitation associated with the local within-catchment trajectories made the largest contribution at CHK (70%) and AA (73%), respectively. We attributed the high contribution of local sources to continuing evapotranspiration on the plains of Uzbekistan where temperatures remain mostly positive in winter. There was uncertainty about the separation of the locally formed precipitation from that forming over the Aral basin in CHK because the catchment is a part of the Aral basin with extensive irrigation. The westerly group made the largest contribution in UA, located on the northernmost slope of the Tien Shan, in JJA (49%) and DJF (54%) and in AA in all seasons (46-50%) except DJF.

The combined back trajectory and mixing model analysis has several limitations. Firstly, the performance of the mixing model depends on the differences in isotopic signatures between the trajectory clusters (Fig. 7) and groups (Fig. 8). This separation was less clear in MAM (Fig. 8) when precipitation maximum is observed increasing uncertainty in this season. Secondly, while the trajectory method determines provenance of the air masses, it does not account for moisture uptake along the transportation routes. However, our results were consistent with Wang et al. (2017) who used back trajectories adjusted using specific humidity and showed that the terrestrial moisture evaporated from Europe and CA may be the main source of precipitation in the Chinese Tien Shan. The results were also consistent with the outcomes of the moisture-tracking models. Tuinenburg et al. (2020) showed that evaporation recycling (defined as the fraction of evaporation that precipitates in the same river basin it is evaporated from) reaches 30-40% over the Tien Shan and its foothills. The annual mean of the distance which evaporated moisture travelled in a longitudinal direction is about 2-6° (Tuinenburg et al., 2020) which is consistent with the length of the local trajectories (Table 2). Application of a specific humidity-based model (e.g., Oza et al., 2022; Natali et al., 2023) would be a useful follow-on study to account for the history of moisture dynamics along the trajectories.

The third limitation was the discrepancy between the number of the identified trajectory clusters and the number of components in the mixing model imposed by the use of two tracers. To overcome this, Clusters 1, 2 and 3 were merged to form Group 1 'Westerly'. This problem did not affect the CKS and CHK catchments where Group 1 was represented by a single cluster (Fig. S2). In AA clusters were merged to form Group 1 in MAM (Clusters 1 and 2 had six and two members, respectively) and SON (Clusters 1 and 2 had one and seven members, respectively). Five clusters were represented in the UA catchment only. However, there was clear seasonality in cluster occurrence at this site. The trajectory of a single precipitation event was assigned to Cluster 1 in DJF and there was no statistically significant difference between Clusters 2 and 3 (p=0.29) forming Group 1. By contrast, the difference between Groups 1, 2 and 3 was significant at 93% confidence level for $\delta^{18}O$ (Fig. S2). In JJA, Group 1 included 61 events assigned to Cluster 1. The different between Clusters 2 and 3 for $\delta^{18}O$ was statistically

significant (p=0.03) but a small number of events (3 and 6, respectively) was assigned to these clusters. The difference with Cluster 1 was significant at 91% confidence level. In SON, Cluster 1 included 18 events and the difference with Clusters 2 (n=2) and 3 (n=5) was not statistically significant (p=0.13). Therefore, the uncertainty imposed by the limitation of the methodology is moderated by the seasonality of clusters at the UA catchment because a single cluster dominates in Group 1 in each season. In the future, this problem will be overcome by using electric conductivity of precipitation as an additional tracer in the mixing model.

The identified significant contribution of the local sources and the extensively irrigated lower reaches of the Amu Darya and Syr Darya as well as over 80 artificial reservoirs located in this region (Xenarios et al., 2019) to precipitation in the Tien Shan poses questions about the effects of both climate change including the observed and projected increase in evaporation (Ren et al., 2022; Tuinenburg et al., 2020) and water management (Wei et al., 2013) on moisture cycling in CA. Regional evapotranspiration was previously shown to provide a significant input in precipitation especially during dry periods in the arid and semi-arid regions globally (Miralles et al., 2016). Water evaporated from the irrigated land contributes to precipitation over the glacierized UA and CKS catchments (and possibly CHK) contributing to snow accumulation at high elevations in MAM which is the main accumulation season in the region. This, in turn, sustains seasonal snowpack and glaciers providing water for irrigation. A modelling study by de Kok et al. (2018) suggested that increased irrigation in the Tarim basin altered precipitation regime in a way that favoured glacier growth in the Kunlun Shan providing partial explanation to the formation of the Karakorum-Kunlun-east Pamir anomaly (Farinotti et al., 2020). Our analysis of isotopic composition of precipitation shows that the same mechanism may operate in some regions of the Tien Shan.

5 Conclusions

An important achievement of this study is the development of an extensive database of precipitation ratios and *d-excess* for the mountains of CA. These data have enabled analysis of geographical, elevational, and temporal patterns in precipitation isotopic composition, and the attribution of precipitation to regional sources. Contributing these data to GNIP will improve the representation of the CA mountains in the global high-resolution precipitation isoscapes databases, especially in the cold season when the differences between modelled and measured ratios were highest. The advantages of the developed dataset are: (i) a wide geographical coverage from the northern Tien Shan to the Gissar-Alay foothills; (ii) sampling at different elevations within two catchments because of the limited availability of such data globally; and (iii) availability of the event-based precipitation samples. The legacy of the programme is the installation of the Palmex Rain Samplers for the long-term collection of monthly precipitation samples for isotopic analysis in three catchments (Kishi Almaty, CKS, and CHK) including samplers at two elevations (700 m and 3438 m a.s.l. and away from the lake in the neighbour catchment of UA) in the Kishi Almaty catchment which will support further investigation in elevational gradients in isotopic ratios and *d-excess*.

Clear annual cycles in $\delta^{18}O$ and δD were identified with maxima in summer and minima in winter at all sites, while annual *d-excess* cycles highlighted the effects of local conditions on precipitation formation. Both $\delta^{18}O$ and δD values increase from north to south. These temporal and spatial patterns and the regression between air temperature and isotopic ratios showed that local air temperature controls the isotopic composition of precipitation. The relationships between $\delta^{18}O$ and δD and geographical variables were quantified, though further investigation including a combined data set from CA and the Chinese Tien Shan will likely enhance result robustness.

LMWLs were developed for the whole region and for individual catchments and seasons. The use of the weighted precipitation and the PWLSR method to derive LMWLs is recommended in JJA especially in the southern part of the region, while unweighted precipitation can be used in other seasons and in the northern Tien Shan using OLSR and RMA methods.

For the first time, the isotopologue data were used together with back trajectories to determine the contribution of different trajectory sources to precipitation. It was shown that the combined contribution of inland re-evaporated moisture from the irrigated land in the Aral basin and local moisture recycling exceeded the contribution of the longer-distance transport associated with the westerlies. The model has several limitations and the following improvements will be needed to confirm the initial findings: a longer sampling period enabling better separation between trajectory clusters, accounting for the history of moisture uptake along the transportation routes, and the application of additional tracers to increase the number of end members in the mixing model. However, the identified contribution of re-evaporated moisture to regional precipitation highlights strong water loss and inefficient water management in CA. It also suggests that irrigation sustained by snow and glacier melt and associated increase in evapotranspiration may benefit glacier mass balance, an issue which requires further investigation. Further work to improve the spatial density of sampling sites and increase the number of samples, especially in the inner Tien Shan and the Pamir, is also needed to confirm the findings.

Acknowledgements

This work was supported by the UK Global Challenges Research Fund (GCRF). Project *'Central Asia Research and Adaptation Water Network (CARAWAN)'* supported the sampling programme across the region. Project *'Solutions for Clean Water in Central Asia: What Happens After the Ice? (SCWAI)'* supported sample processing and analysis. The sampling programme in Kazakhstan was additionally supported by the Science Committee of the Ministry of Science and Higher Education of the Republic of Kazakhstan (Grant No. BR18574176). Zarina Saidaliyeva was supported by the University of Reading International PhD Studentship. The authors are grateful to the anonymous referees for their most helpful comments.

Authors' contributions

MS, ZS, AW, and VY conceptualised the study; ZS processed samples and analysed the data, MS and AW supervised; ZS and MS wrote the original manuscript. Other authors participated in the sampling programme and provided meteorological data. All authors contributed to the discussion of results and the final version of the manuscript.

Competing interests

The authors declare that they have no conflict of interest.

References

Aemisegger, F., Pfahl, S., Sodemann, H., Lehner, I., Seneviratne, S. I., and Wernli, H.: Deuterium excess as a proxy for continental moisture recycling and plant transpiration, Atmos. Chem. Phys., 14, 4029–4054, https://doi.org/10.5194/acp-14-4029-2014, 2014.

Aggarwal, P. K., Romatschke, U., Araguas-Araguas, L., Belachew, D., Longstaffe, F. J., Berg, P., Schumacher, C., and Funk, A.: Proportions of convective and stratiform precipitation revealed in water isotope ratios, Nat. Geosci., 9, 624–629, https://doi.org/10.1038/ngeo2739, 2016.

Aizen, E. M., Aizen, V. B., Mayewski, P. A., Zhou, H., Rodda, C., Joswiak, D., Takeuchi, N., Fujita, K., Kurbatov, A., and Grigholm, B. O.: Aridity of Central Asia through the Holocene, 2017, GC41G-02, 2017.

Aizen, V., Aizen, E., Melack, J., and Martma, T.: Isotopic measurements of precipitation on central Asian glaciers (southeastern Tibet, northern Himalayas, central Tien Shan), J. Geophys. Res. Atmos., 101, 9185–9196,

https://doi.org/10.1029/96JD00061, 1996.

Aizen, V. B., Aizen, E. M., and Melack, J. M.: Snow distribution and melt in central Tien Shan, susamir valley, Arct. Alp.
700 Res., 29, 403–413, https://doi.org/10.2307/1551988, 1997.

Aizen, V. B., Aizen, E. M., Melack, J. M., Kreutz, K. J., and Cecil, L. D. W.: Association between atmospheric circulation
patterns and firn-ice core records from the Inilchek glacierized area, central Tien Shan, Asia, J. Geophys. Res. D Atmos.,
109, https://doi.org/10.1029/2003JD003894, 2004.

Aizen, V. B., Mayewski, P. A., Aizen, E. M., Joswiak, D. R., Surazakov, A. B., Kaspari, S., Grigholm, B., Krachler, M.,
705 Handley, M., and Finaev, A.: Stable-isotope and trace element time series from Fedchenko glacier (Pamirs) snow/firn cores,
J. Glaciol., 55, 275–291, https://doi.org/10.3189/002214309788608787, 2009.

Araguás-Araguás, L., Froehlich, K., and Rozanski, K.: Deuterium and oxygen-18 isotope composition of precipitation and
atmospheric moisture, Hydrol. Process., 14, 1341–1355, https://doi.org/10.1002/1099-1085(20000615)14:8<1341::AID-
HYP983>3.3.CO;2-Q, 2000.

710 Bagheri, R., Bagheri, F., Karami, G. H., and Jafari, H.: Chemo-isotopes (18O & 2H) signatures and HYSPLIT model
application: Clues to the atmospheric moisture and air mass origins, Atmos. Environ., 215, 116892,
https://doi.org/10.1016/j.atmosenv.2019.116892, 2019.

Bershaw, J.: Controls on deuterium excess across Asia, Geosci., 8, https://doi.org/10.3390/geosciences8070257, 2018.

Bowen, G. J.: Isoscapes: Spatial Pattern in Isotopic Biogeochemistry, Annu. Rev. Earth Planet. Sci., 38, 161–187,
715 https://doi.org/10.1146/annurev-earth-040809-152429, 2010.

Bowen, G. J.: The Online Isotopes in Precipitation Calculator, version OIPC3.1. http://www.waterisotopes.org, 2022.

Bowen, G. J., Kennedy, C. D., Henne, P. D., and Zhang, T.: Footprint of recycled water subsidies downwind of Lake
Michigan, 3, art53, https://doi.org/10.1890/ES12-00062.1, 2012.

Bowen, G. J., Putman, A., Brooks, J. R., Bowling, D. R., Oerter, E. J., and Good, S. P.: Inferring the source of evaporated
720 waters using stable H and O isotopes, Oecologia, 187, 1025–1039, https://doi.org/10.1007/s00442-018-4192-5, 2018.

Bowen, G. J., Cai, Z., Fiorella, R. P., and Putman, A. L.: Isotopes in the Water Cycle: Regional- to Global-Scale Patterns and
Applications, Annu. Rev. Earth Planet. Sci., 47, 453–479, https://doi.org/10.1146/annurev-earth-053018-060220, 2019.

Chen, F., Wang, S., Wu, X., Zhang, M., Argiriou, A. A., Zhou, X., and Chen, J.: Local Meteoric Water Lines in a Semi-Arid
Setting of Northwest China Using Multiple Methods, 13, 2380, https://doi.org/10.3390/w13172380, 2021.

725 Chen, L., Zhu, G., Lin, X., Li, R., Lu, S., Jiao, Y., Qiu, D., Meng, G., and Wang, Q.: The Complexity of Moisture Sources
Affects the Altitude Effect of Stable Isotopes of Precipitation in Inland Mountainous Regions, Water Resour. Res., 60,
https://doi.org/10.1029/2023WR036084, 2024.

Consortium, R.: Randolph glacier inventory–a dataset of global glacier outlines: Version 6.0: technical report, global land ice
measurements from space, Colorado, USA, Digit. Media. https//doi. org/10.7265, 2017.

730 Craig, H.: Isotopic Variations in Meteoric Waters, Science (80-.)., 133, 1702–1703,
https://doi.org/10.1126/science.133.3465.1702, 1961.

Craig, H. and Gordon, L.: Deuterium and oxygen 18 variations in the ocean and the marine atmosphere, 9–130 pp., 1965.

Crawford, J., Hughes, C. E., and Lykoudis, S.: Alternative least squares methods for determining the meteoric water line, demonstrated using GNIP data, J. Hydrol., 519, 2331–2340, https://doi.org/10.1016/j.jhydrol.2014.10.033, 2014.

735   Dansgaard, W.: Stable isotopes in precipitation, Tellus A Dyn. Meteorol. Oceanogr., 16, 436, https://doi.org/10.3402/tellusa.v16i4.8993, 1964.

Dorling, S. R., Davies, T. D., and Pierce, C. E.: Cluster analysis : a technique for estimating the synoptic meteorological controls on air and precipitation chemistry--results from Eskdalemuir, South Scotland, Atmos. Environ., 26, 2583–2602, 1992.

740   Draxler, R. R. and Rolph, G. D.: HYSPLIT (HYbrid Single-Particle Lagrangian Integrated Trajectory) Model access via NOAA ARL READY Website, NOAA Air Resour. Lab. Silver Spring, MD, http://ready.arl.noaa.gov/HYSPLIT.php, 2013.

Van Der Ent, R. J. and Tuinenburg, O. A.: The residence time of water in the atmosphere revisited, Hydrol. Earth Syst. Sci., 21, 779–790, https://doi.org/10.5194/hess-21-779-2017, 2017.

Farinotti, D., Longuevergne, L., Moholdt, G., Duethmann, D., Mölg, T., Bolch, T., Vorogushyn, S., and Güntner, A.:
745   Substantial glacier mass loss in the Tien Shan over the past 50 years, Nat. Geosci., 8, 716–722, https://doi.org/10.1038/ngeo2513, 2015.

Farinotti, D., Immerzeel, W. W., de Kok, R. J., Quincey, D. J., and Dehecq, A.: Manifestations and mechanisms of the Karakoram glacier Anomaly, Nat. Geosci., 13, 8–16, https://doi.org/10.1038/s41561-019-0513-5, 2020.

Friedman, I., Machta, L., and Soller, R.: Water-vapor exchange between a water droplet and its environment, J. Geophys.
750   Res., 67, 2761–2766, https://doi.org/10.1029/JZ067i007p02761, 1962.

Froehlich, K., Kralik, M., Papesch, W., Rank, D., Scheifinger, H., and Stichler, W.: Deuterium excess in precipitation of Alpine regions – moisture recycling, Isotopes Environ. Health Stud., 44, 61–70, https://doi.org/10.1080/10256010801887208, 2008.

Gat, J. R.: Oxygen and Hydrogen Isotopes in the Hydrologic Cycle, Annu. Rev. Earth Planet. Sci., 24, 225–262,
755   https://doi.org/10.1146/annurev.earth.24.1.225, 1996.

Gat, J. R. and Gonfiantini, R.: Stable Isotope Hydrology Deuterium and Oxygen-18 in the Water Cycle. Inte, rnational At. energy agency, 339, 1981.

He, Z., Unger-shayesteh, K., Vorogushyn, S., Weise, S. M., Kalashnikova, O., Gafurov, A., Duethmann, D., Barandun, M., and Merz, B.: Constraining hydrological model parameters using water isotopic compositions in a glacierized basin , Central
760   Asia, 571, 332–348, https://doi.org/10.1016/j.jhydrol.2019.01.048, 2019.

Hoelzle, M., Barandun, M., Bolch, T., Fiddes, J., Gafurov, A., Muccione, V., Saks, T., and Shahgedanova, M.: The status and role of the alpine cryosphere in Central Asia, Aral Sea Basin Water Sustain. Dev. Cent. Asia, 2, 100–121, https://doi.org/10.4324/9780429436475-8, 2019.

Hughes, C. E. and Crawford, J.: A new precipitation weighted method for determining the meteoric water line for
765   hydrological applications demonstrated using Australian and global GNIP data, J. Hydrol., 464–465, 344–351, https://doi.org/10.1016/j.jhydrol.2012.07.029, 2012.

IAEA/WMO: Global Network of Isotopes in Precipitation. The GNIP Database. Accessible at: https://nucleus.iaea.org/wiser., 2015.

Immerzeel, W. W., Lutz, A. F., Andrade, M., Bahl, A., Biemans, H., Bolch, T., Hyde, S., Brumby, S., Davies, B. J., Elmore,
A. C., Emmer, A., Feng, M., Fernández, A., Haritashya, U., Kargel, J. S., Koppes, M., Kraaijenbrink, P. D. A., Kulkarni, A.
V., Mayewski, P. A., Nepal, S., Pacheco, P., Painter, T. H., Pellicciotti, F., Rajaram, H., Rupper, S., Sinisalo, A., Shrestha,
A. B., Viviroli, D., Wada, Y., Xiao, C., Yao, T., and Baillie, J. E. M.: Importance and vulnerability of the world's water
towers, Nature, 577, 364–369, https://doi.org/10.1038/s41586-019-1822-y, 2020.

Jasechko, S.: Global Isotope Hydrogeology—Review, Rev. Geophys., 57, 835–965, https://doi.org/10.1029/2018RG000627,
2019.

Jiang, J., Zhou, T., Chen, X., and Zhang, L.: Future changes in precipitation over Central Asia based on CMIP6 projections,
Environ. Res. Lett., 15, https://doi.org/10.1088/1748-9326/ab7d03, 2020.

Jin, L., Chen, F., Morrill, C., Otto-Bliesner, B. L., and Rosenbloom, N.: Causes of early Holocene desertification in arid
central Asia, Clim. Dyn., 38, 1577–1591, https://doi.org/10.1007/s00382-011-1086-1, 2012.

Jorba, O., Pérez, C., Rocadenbosch, F., and Baldasano, J.: Cluster Analysis of 4-Day Back Trajectories Arriving in the
Barcelona Area, Spain, from 1997 to 2002, J. Appl. Meteorol., 43, 887–901, https://doi.org/10.1175/1520-
0450(2004)043<0887:CAODBT>2.0.CO;2, 2004.

Juhlke, T. R., Meier, C., Van Geldern, R., Vanselow, K. A., Wernicke, J., Baidulloeva, J., Barth, J. A. C., and Weise, S. M.:
Assessing moisture sources of precipitation in the Western Pamir Mountains (Tajikistan, Central Asia) using deuterium
excess, Tellus B Chem. Phys. Meteorol., 71, 1601987, https://doi.org/10.1080/16000889.2019.1601987, 2019.

Kapitsa, V., Shahgedanova, M., Severskiy, I., Kasatkin, N., White, K., and Usmanova, Z.: Assessment of Changes in Mass
Balance of the Tuyuksu Group of Glaciers, Northern Tien Shan, Between 1958 and 2016 Using Ground-Based Observations
and Pléiades Satellite Imagery, Front. Earth Sci., 8, https://doi.org/10.3389/feart.2020.00259, 2020.

Kaser, G., Großhauser, M., and Marzeion, B.: Contribution potential of glaciers to water availability in different climate
regimes, Proc. Natl. Acad. Sci. U. S. A., 107, 20223–20227, https://doi.org/10.1073/pnas.1008162107, 2010.

de Kok, R. J., Tuinenburg, O. A., Bonekamp, P. N. J., and Immerzeel, W. W.: Irrigation as a Potential Driver for Anomalous
Glacier Behavior in High Mountain Asia, Geophys. Res. Lett., 45, 2047–2054, https://doi.org/10.1002/2017GL076158,
2018.

Kostrova, S. S., Meyer, H., Fernandoy, F., Werner, M., and Tarasov, P. E.: Moisture origin and stable isotope characteristics
of precipitation in southeast Siberia, Hydrol. Process., 34, 51–67, https://doi.org/10.1002/hyp.13571, 2020.

Kreutz, K. J., Wake, C. P., Aizen, V. B., DeWayne Cecil, L., and Synal, H. A.: Seasonal deuterium excess in a Tien Shan ice
core: Influence of moisture transport and recycling in Central Asia, Geophys. Res. Lett., 30,
https://doi.org/10.1029/2003GL017896, 2003.

Kutuzov, S. and Shahgedanova, M.: Glacier retreat and climatic variability in the eastern Terskey-Alatoo, inner Tien Shan
between the middle of the 19th century and beginning of the 21st century, Glob. Planet. Change, 69, 59–70,
https://doi.org/10.1016/j.gloplacha.2009.07.001, 2009.

Lachniet, M. S. and Patterson, W. P.: Use of correlation and stepwise regression to evaluate physical controls on the stable
isotope values of Panamanian rain and surface waters, J. Hydrol., 324, 115–140,
https://doi.org/10.1016/j.jhydrol.2005.09.018, 2006.

Liu, J., Song, X., Yuan, G., Sun, X., and Yang, L.: Stable isotopic compositions of precipitation in China, Tellus B Chem.

Phys. Meteorol., 66, 22567, https://doi.org/10.3402/tellusb.v66.22567, 2014.

Lydolph, P. E.: Climates of the Soviet Union, edited by: Paul E. Lydolph and Landsberg, H. E., Elsevier Scientific Publishing Company, 443 pp., 1977.

Minder, J. R., Bartolini, W. M., Spence, C., Hedstrom, N. R., Blanken, P. D., and Lenters, J. D.: Characterizing and constraining uncertainty associated with surface and boundary layer turbulent fluxes in simulations of lake-effect snowfall, Weather Forecast., 35, 467–488, https://doi.org/10.1175/WAF-D-19-0153.1, 2020.

Miralles, D. G., Nieto, R., McDowell, N. G., Dorigo, W. A., Verhoest, N. E. C., Liu, Y. Y., Teuling, A. J., Dolman, A. J., Good, S. P., and Gimeno, L.: Contribution of water-limited ecoregions to their own supply of rainfall, Environ. Res. Lett., 11, https://doi.org/10.1088/1748-9326/11/12/124007, 2016.

Natali, S., Doveri, M., Giannecchini, R., Baneschi, I., and Zanchetta, G.: Is the deuterium excess in precipitation a reliable tracer of moisture sources and water resources fate in the western Mediterranean? New insights from Apuan Alps (Italy), J. Hydrol., 614, https://doi.org/10.1016/j.jhydrol.2022.128497, 2022.

Natali, S., Doveri, M., Franceschi, L., Giannecchini, R., Luppichini, M., Menichini, M., and Zanchetta, G.: Moisture sources and climatic effects controlling precipitation stable isotope composition in a western Mediterranean island (Pianosa, Italy), Atmos. Res., 294, 106987, https://doi.org/10.1016/j.atmosres.2023.106987, 2023.

Oza, H., Padhya, V., Ganguly, A., and Deshpande, R. D.: Investigating hydrometeorology of the Western Himalayas: Insights from stable isotopes of water and meteorological parameters, Atmos. Res., 268, 105997, https://doi.org/10.1016/j.atmosres.2021.105997, 2022.

Pang, Z., Kong, Y., Froehlich, K., Huang, T., Yuan, L., Li, Z., and Wang, F.: Processes affecting isotopes in precipitation of an arid region, Tellus B Chem. Phys. Meteorol., 63, 352, https://doi.org/10.1111/j.1600-0889.2011.00532.x, 2011.

Pérez, I. A., Artuso, F., Mahmud, M., Kulshrestha, U., Sánchez, M. L., and García, M. Á.: Applications of Air Mass Trajectories, Adv. Meteorol., 2015, 1–20, https://doi.org/10.1155/2015/284213, 2015.

Phillips, D. L. and Gregg, J. W.: Uncertainty in source partitioning using stable isotopes, Oecologia, 127, 171–179, https://doi.org/10.1007/s004420000578, 2001.

Putman, A. L., Fiorella, R. P., Bowen, G. J., and Cai, Z.: A Global Perspective on Local Meteoric Water Lines: Meta-analytic Insight Into Fundamental Controls and Practical Constraints, Water Resour. Res., 55, 6896–6910, https://doi.org/10.1029/2019WR025181, 2019.

Ren, Y., Yu, H., Liu, C., He, Y., Huang, J., Zhang, L., Hu, H., Zhang, Q., Chen, S., Liu, X., Zhang, M., Wei, Y., Yan, Y., Fan, W., and Zhou, J.: Attribution of Dry and Wet Climatic Changes over Central Asia, J. Clim., 35, 1399–1421, https://doi.org/10.1175/JCLI-D-21-0329.1, 2022.

Rolph, G., Stein, A., and Stunder, B.: Real-time Environmental Applications and Display sYstem: READY, Environ. Model. Softw., 95, 210–228, https://doi.org/10.1016/j.envsoft.2017.06.025, 2017.

Rozanski, K., Araguás-Araguás, L., and Gonfiantini, R.: Isotopic Patterns in Modern Global Precipitation, in: Journal of Geophysical Research Atmospheres, 1–36, https://doi.org/10.1029/GM078p0001, 2013.

Severskiy, I., Vilesov, E., Armstrong, R., Kokarev, A., Kogutenko, L., Usmanova, Z., Morozova, V., and Raup, B.: Changes in glaciation of the Balkhash–Alakol basin, central Asia, over recent decades, Ann. Glaciol., 57, 382–394, https://doi.org/10.3189/2016AoG71A575, 2016.

Shahgedanova, M.: In: The Physical Geography of Northern Eurasia: Russia and Neighbouring States., in: Climate at Present and in the Historical Past., Oxford University Press, 70–102, 2002.

845 Shahgedanova, M., Afzal, M., Severskiy, I., Usmanova, Z., Saidaliyeva, Z., Kapitsa, V., Kasatkin, N., and Dolgikh, S.: Changes in the mountain river discharge in the northern Tien Shan since the mid-20th Century: Results from the analysis of a homogeneous daily streamflow data set from seven catchments, J. Hydrol., 564, 1133–1152, https://doi.org/10.1016/j.jhydrol.2018.08.001, 2018.

Stein, A. F., Draxler, R. R., Rolph, G. D., StundeR, B. J. B., Cohen, M. D., and Ngan, F.: Noaa's hysplit atmospheric
850 transport and dispersion modeling system, Bull. Amer. Meteor. Soc., 96, 2059–2078, https://doi.org/https://doi.org/10.1175/BAMS-D-14-00110.1, 2015.

Tian, L., Yao, T., MacClune, K., White, J. W. C., Schilla, A., Vaughn, B., Vachon, R., and Ichiyanagi, K.: Stable isotopic variations in west China: A consideration of moisture sources, J. Geophys. Res. Atmos., 112, 1–12, https://doi.org/10.1029/2006JD007718, 2007.

855 Tuinenburg, O. A., Theeuwen, J. J. E., and Staal, A.: High-resolution global atmospheric moisture connections from evaporation to precipitation, Earth Syst. Sci. Data, 12, 3177–3188, https://doi.org/10.5194/essd-12-3177-2020, 2020.

Viviroli, D., Kummu, M., Meybeck, M., Kallio, M., and Wada, Y.: Increasing dependence of lowland populations on mountain water resources, Nat. Sustain., https://doi.org/10.1038/s41893-020-0559-9, 2020.

Wang, L., Dong, Y., Han, D., and Xu, Z.: Stable isotopic compositions in precipitation over wet island in Central Asia, J.
860 Hydrol., 573, 581–591, https://doi.org/10.1016/j.jhydrol.2019.04.005, 2019.

Wang, S., Zhang, M., Che, Y., Chen, F., and Qiang, F.: Contribution of recycled moisture to precipitation in oases of arid central Asia: A stable isotope approach, Water Resour. Res., 52, 3246–3257, https://doi.org/10.1002/2015WR018135, 2016a.

Wang, S., Zhang, M., Hughes, C. E., Zhu, X., Dong, L., Ren, Z., and Chen, F.: Factors controlling stable isotope
865 composition of precipitation in arid conditions: an observation network in the Tianshan Mountains, central Asia, Tellus B Chem. Phys. Meteorol., 68, 26206, https://doi.org/10.3402/tellusb.v68.26206, 2016b.

Wang, S., Zhang, M., Crawford, J., Hughes, C. E., Du, M., and Liu, X.: The effect of moisture source and synoptic conditions on precipitation isotopes in arid central Asia, J. Geophys. Res. Atmos., 122, 2667–2682, https://doi.org/10.1002/2015JD024626, 2017.

870 Wang, S., Zhang, M., Hughes, C. E., Crawford, J., Wang, G., Chen, F., Du, M., Qiu, X., and Zhou, S.: Meteoric water lines in arid Central Asia using event-based and monthly data, J. Hydrol., 562, 435–445, https://doi.org/10.1016/j.jhydrol.2018.05.034, 2018.

Wang, S., Wang, L., Zhang, M., Shi, Y., Hughes, C. E., Crawford, J., Zhou, J., and Qu, D.: Quantifying moisture recycling of a leeward oasis in arid central Asia using a Bayesian isotopic mixing model, J. Hydrol., 613, 128459,
875 https://doi.org/10.1016/j.jhydrol.2022.128459, 2022.

Wassenaar, L., Terzer-Wassmuth, S., and Douence, C.: Progress and challenges in dual- and triple-isotope (δ18O, δ2H, Δ17O) analyses of environmental waters: An international assessment of laboratory performance, Rapid Commun. Mass Spectrom., 35, 1–12, https://doi.org/10.1002/rcm.9193, 2021.

Wei, J., Dirmeyer, P. A., Wisser, D., Bosilovich, M. G., and Mocko, D. M.: Where Does the Irrigation Water Go? An

880   Estimate of the Contribution of Irrigation to Precipitation Using MERRA, J. Hydrometeorol., 14, 275–289, https://doi.org/10.1175/JHM-D-12-079.1, 2013.

Wu, H., Zhang, X., Xiaoyan, L., Li, G., and Huang, Y.: Seasonal variations of deuterium and oxygen-18 isotopes and their response to moisture source for precipitation events in the subtropical monsoon region, Hydrol. Process., 29, 90–102, https://doi.org/10.1002/hyp.10132, 2015.

885   Xenarios, S., Schmidt-Vogt, D., Qadir, M., Janusz-Pawletta, B., and Abdullaev, I. (Eds.): The Aral Sea Basin. Water for sustainable development in Central Asia, Routledge, 227 pp., https://doi.org/10.4324/9780429436475, 2019.

Xiao, W., Lee, X., Hu, Y., Liu, S., Wang, W., Wen, X., Werner, M., and Xie, C.: An Experimental Investigation of Kinetic Fractionation of Open-Water Evaporation Over a Large Lake, J. Geophys. Res. Atmos., 122, 11,651-11,663, https://doi.org/10.1002/2017JD026774, 2017.

890   Yang, X., Acharya, S., and Yao, T.: Vertical Profile of Meteoric and Surface-Water Isotopes in Nepal Himalayas to Everest's Summit, Atmosphere (Basel)., 14, 202, https://doi.org/10.3390/atmos14020202, 2023.

Yapiyev, V., Skrzypek, G., Verhoef, A., Macdonald, D., and Sagintayev, Z.: Between boreal Siberia and arid Central Asia – Stable isotope hydrology and water budget of Burabay National Nature Park ecotone (Northern Kazakhstan), J. Hydrol. Reg. Stud., 27, 100644, https://doi.org/10.1016/j.ejrh.2019.100644, 2020.

895   Yoshimura, K.: Stable water isotopes in climatology, meteorology, and hydrology: A review, J. Meteorol. Soc. Japan, 93, 513–533, https://doi.org/10.2151/jmsj.2015-036, 2015.

Zhang, M. and Wang, S.: Precipitation isotopes in the Tianshan Mountains as a key to water cycle in arid central Asia, Sci. Cold Arid Reg., https://doi.org/10.3724/SP.J.1226.2018.00027, 2018.

Zongxing, L., Qi, F., Song, Y., Wang, Q. J., Yang, J., Yongge, L., Jianguo, L., and Xiaoyan, G.: Stable isotope composition
900   of precipitation in the south and north slopes of Wushaoling Mountain, northwestern China, Atmos. Res., 182, 87–101, https://doi.org/10.1016/j.atmosres.2016.07.023, 2016.